Effectiveness of Slippery Liquid Infused Porous Surface in Viscous Drag Reduction in Boundary Layers at Varying Reynolds Numbers

Svetlana Pencheva

A thesis submitted to Auckland University of Technology in fulfilment of the requirements for the degree of Doctor of Philosophy (PhD)

2021

School of Engineering and Design

Thesis Abstract

Drag in marine vehicles is unavoidable but a decrease of the drag is always a perused aim. With modern technologies, it is critical to investigate the new opportunities for achieving reduced drag on the marine vessels and using less fuel to propel them.

This work investigates the effect of Slippery Liquid Infused Porous Surface (SLIPS) on surface-water interaction at varying regimes of flow. This work is focused on understanding the potential effects of SLIPS on drag reduction of water flow over solid surfaces and ships.

The SLIPS used in the process was created on the surface of aluminium 5083 due to the fact that, this material is commonly used in marine industry. The method was based on an existing one but with significant modifications. The microstructure is finer but nano-structure is the same. This is achieved by anodising, boehmiting and infusing with silicon oil.

In order to conduct this investigation a number of experiments were done using well-known methods. These involve measuring and comparing the torque required to rotate a disk with and without treatment as an initial set of tests. Since the flow regime may vary along the radius of the disk, additional experiments were conducted with rotating coaxial cylinders. In the final stage of the study, a model of a boat was towed in the Australian Maritime College basin in Launceston, Tasmania.

Comparison of the required force or torque to move treated and non-treated objects at a specified speed show that drag reduction occurs in laminar or dominantly laminar flow but significantly decreases with increase of the turbulences in the flow. A typical drop in resistance is about 3% to 4.5% for the mean values for rotating disk.

Rotating coaxial cylinders tests show bigger drag reduction for a laminar regime: up to 40%. With the development of the turbulence, it falls to 3% and even lower. An interesting phenomenon was found during the tests associated with the observed vibrations. The reduction in resistance is up to 40% in these conditions but this requires a study that is more detailed and focused on that phenomenon.

The model boat was tested without SLIPS and with SLIPS. Assuming that the residuary resistance is the same in both cases, it was derived from the non-treated boat test and used for calculating the friction resistance of the treated boat.

Using the derived frictional resistance and frictional coefficient from the towing test of the model, a rough estimation was made of the total resistance of the full-size vessel. For the estimated mean frictional resistance drop of 3%, the total resistance of the ship is expected to decrease between 0 to 1.5%.

Key Words: Viscous Drag Reduction, Slippery Liquid Infused Porous Surface, Experimental Analysis

Contents

"I hereby declare that this submission is my own work and that, to the best of my knowledge and belief, it contains no material previously published or written by another person (except where explicitly defined in the acknowledgements), nor material which to a substantial extent has been submitted for the award of any other degree or diploma of a university or other institution of higher learning."

Svetlana Pencheva

25 March 2021

Acknowledgment

In the opening speech of Sixth Conference of Advanced Materials and Nanotechnology professor J. Aizenberg introduced Slippery Lubricant Induced Porous Surfaces and their potential in marine application. This work is inspired by that speech.

I would like to thank my supervisor Professor Dr. Sascha Kosleck, who supported me throughout the entire project and trusted my ability more than I did.

I highly appreciate the enthusiastic encouragement of my second supervisors Dr. John Robertson and Professor Dr. Shuhong Chai, always available and generous with their expertise.

I have to thank the colleagues at AMC Towing Tanks and special thanks to Nick and Gregor for the incredible support I had during the towing experiments.

To my supervisor Professor Dr. Tek Tjing Lie. Your flexibility and understanding made navigating the academia labyrinth manageable, without which this project would not have been possible.

A special thank you goes to the colleagues at Science department for giving me access to the laboratory of Thermodynamics and equipment. Without this I would not be able to complete my project.

I would like to thank my colleagues at Unitec for affording me extra time for my study during the busy school year.

Last but not least, I thank my family: my husband Boris, my mother-in-law Vessie and my adult kids. All of them were extremely supportive and patient with me and my progress.

List of figures

List of tables

Nomenclature

$Re_{\varphi,\ local}$	Local Reynolds number	[-]
$(1+k)$	Form coefficient	[-]
Ω_a	Angular velocity of the inner cylinder	[rad/s]
Ω_b	Angular velocity of the outer cylinder	[rad/s]
C_A	Allowance friction coefficient	[-]
C_F	Friction coefficient of the ship	[-]
C_R	Residuary coefficient	[N]
$C_{T(estimated)}$	Estimated total friction coefficient	[-]
$C_{T(measured)}$	Measured total friction coefficient	[-]
F_n	Froude number	[-]
J^{ω}	Conserved transverse current of rotational motion	[m^4/s^2]
R_{F_M}	Friction resistance of the model	[N]
R_{F_S}	Friction resistance of the ship	[N]
R_A	Resistance component giving allowance	[N]
R_F	Friction resistance of the sip	[N]
R_M	Model resistance	[N]
R_R	Residuary resistance	[N]
R_S	Ship resistance	[N]
R_e	Reynolds number	[-]
R_n	Reynolds number	[-]
T_{am}	Taylor number	[-]
T_q	Torque	[Nm]
p_*	Dimensionless pressure	[-]
$s_{\bar{x}}$	Standard error of the mean	
u_0	Slip velocity	[m/s]
u_{φ}	Velocity of a fluid element in φ direction of polar coordinate system	[m/s]
u_r	Velocity of a fluid element in r direction of polar coordinate system	[m/s]
u_{r*}	Dimensionless radial velocity	[-]
u_x	Velocity of a fluid element in x direction of Cartesian coordinate system	[m/s]
u_y	Velocity of a fluid element in y direction of Cartesian coordinate system	[m/s]
u_z	Velocity of a fluid element in z direction of Cartesian coordinate system	[m/s]
u_{z*}	Dimensionless axial velocity	[-]
$u_{\varphi*}$	Dimensionless azimuth velocity	[-]
$\bar{x}$	Mean value	
x_i	Value of the parameter at an experiment	
z_*	Dimensionless axial location	[-]
θ_c	Critical contact angle	[rad]
μ_{bulk}	Density of the outer layer, bulk	[kg/m^3]
τ_{φ}	Tangential component of shear stress	[Pa]
ϕ_s	Projected area of the textured surface	[m^2]

ϱ_M	Density of water for model testing tank	[kg/m^3]
ϱ_S	Density of water for ship environment	[kg/m^3]
μ_{wall}	Density near wall	[kg/m^3]
boehmite	Aluminium Oxide Hydroxide	
SLIPS	Slippery Liquid Infused Porous Surface	
Γ	Aspect ratio	[-]
Ω	Angular velocity	[rad/s]
A	Area of the surface of the cylinder	[m^2]
G	Dimensionless torque	[-]
H	Inner cylinder length	[m]
L	Length of the ship	[m]
$M\%$	Measured torque in parts per thousands	[‰]
S	Wetted surface of the ship	[m^2]
TN	Torque for non-treated cylinder	[Nm]
TR	Torque percentage change	[%]
TT	Torque for the treated cylinder	[Nm]
V	Velocity of the ship	[m/s]
a	Radius of the inner cylinder	[m]
b	Slip length	[m]
page 8, 9, 13		
b	Radius of the outer cylinder	[m]
d	Gap between coaxial cylinders	[m]
i	Identifying number for each experiment	
n	Number of experiments	
p	Pressure	[Pa]
r	Local radius	[m]
s	Standard deviation of the sample	
t	Time	[s]
u	Velocity	[m/s]
δ	Layer thickness	[m]
η	Radius ratio	[-]
λ	Ship-model scale factor	[-]
μ	Viscosity	[Pa s]
ν	Kinematic viscosity	[m^2/s]
ρ	Density	[kg/m^3]
τ	Viscous shear stress	[Pa]
φ	Azimuth angle of polar coordinate system	[rad]
ω	Angular velocity	[rad/s]

Chapter

1. Introduction

A ship's resistance is governed by many factors, which interact in a complex way. Naval architects, consider four main components, wave making, eddy resistance, air resistance and frictional resistance in water. The latter is associated with the properties of water and the surface of the ship hull. Wave making and eddy resistance, often combined in the term residuary resistance, are known as shape dependent and are not a subject of this research. However, the surface of the ship requires a new assessment when using new technologies of treatment and/or coatings. These technologies may provide new qualities which lead to a decrease in friction and environmentally friendly antifouling.

The new surfaces, like those with the well-known lotus effect, have proven to decrease resistance. They are textured on a nano-scale order. The effect can be based on air entrapped under a water drop. Unfortunately, that ability is quickly lost when under a solid sheet of water and applied pressure. Another variation developed is a lubricant-filled nano-structured surface. The resulting effects are anti freezing in some cases, or self-cleaning and self-repairing abilities. These are usually tested in aerated environment but not in conditions of solid water flow and not under pressure.

This study focuses on applying of one of these new technologies to marine applications. The work investigates the effect of these surfaces on surface-water interaction at varying regimes of flow, as well as on the overall resistance of the ship.

The general reduction of drag in fluid flows is beneficial to a huge variety of industries. For instance a ten per cent reduction of the drag for merchant vessels may lead to billions of dollars savings per year in the shipping industry alone (Woo Yang et al., 2014), as it

reduces fuel consumption and emissions. The same applies for applications in which a liquid transfer through piping systems is required. Every reduction in drag leads to savings in energy consumption and is therefore cost efficient and eco-friendly.

This explains the extensive work in this area over the last 50-60 years, with varying degree of success. Gas injection was a promising method with a number of reports suggesting a good amount of reduction in skin friction. (Fukuda et al., 2000; Murai, Fukuda, Oishi, Kodama, & Yamamoto, 2007; Sverchkov, 2010) A tool was developed for micro-bubble drag reduction prediction. (Kunz et al., 2006)

In contrast to that success, members of the Maritime Research Institute of the Netherlands reported that the energy saving due to the effect of air lubrication is negated by the energy required to produce that effect. (Foeth, 2010)

Polymer additives are an alternative method that works well in pipes but polymer injection in watercraft implies the need for hull penetrations and a system for the process of injection. Some paints, which release polymers, have recently been developed. (Woo Yang et al., 2014)

Compliant coatings imitate dolphin skin. They are supposed to respond to the flow in a favourable way resulting in a delay of the laminar to turbulent flow transition. This reduces skin friction by up to 8%. (Bushnell, Hefner, & ebrary Inc., 1990; Fujimtsu, 2013; Gad-el-Hak, 2002) On the other hand, in 2005 a combined team from the UK, USA and Russia published results of their experiments on the “effects of aging on compliant coating drag reduction”. They reported that viscoelastic properties and drag reduction generally deteriorate with the aging of the coatings, probably, due to crosslinking i.e. naturally-occurring chemical bonds between the long molecules.

The use of riblets is another nature mimic technique. This microstructure along the flow stream imitates sharkskin and is effective for turbulent flow when the vortices are lifted up and pinned to the tip of the riblets. The effect of drag reduction is highly dependent on the design of these structures where specific flow velocities play a dramatic role. (Bhushan, 2012; Bixler & Bhushan, 2013)

Technological developments bring to life new materials and surfaces. It is critical to explore their quality and ability to reduce drag alone or in combination with other techniques. Slippery Liquid Infused Porous Surface (SLIPS) is such a new innovative development by the team led by Joanna Aizenberg who introduced it at the Sixth International Conference of Advanced Materials and Nanotechnology in Auckland. There are indications that it is suitable for drag reduction and possibly resistant to bio fouling. (Bhushan, 2012; P. Kim, Michael J. Kreder, Jack Alvarenga, & Joanna Aizenberg, 2013b)

The aim of this work is to deliver an improved understanding of the potential effects of SLIPS on drag reduction of water flow over solid surfaces and ships.

In the process of choosing suitable methods of testing SLIPS for drag reduction number of options were considered. Section 2. 4. deals with this assessment in details. Finally, it was decided to run rotating disk experiment for initial assessment due to the easy access to the device and well-known theoretical framework, which offers good reliability assessment. The assessment is made by comparing the applied torque for rotating a disk with and without SLIPS.

While rotating disk is a quick but too general assessment, a better-specified condition has to be used in this study. Rotating cylinder experiment, section 5. 4, provides this opportunity in laboratory situation. Similarly, to rotating disk experiment, it is accessible and reliable. It does not require expensive equipment and other sophisticated resources.

Towing tank experiment is a logical testing method when exploring marine application of SLIPS. Chapter 6 is dealing with this experiment. A boat model with an overall length of 1.25 m with SLIPS applied is tested in a towing tank at number of different cruising speeds. Measured towing forces are compared with corresponding forces from similar tests where the surface of the boat does not include SLIPS.

1. 1. Structure of the thesis

The thesis starts with the literature review in Chapter 2, which introduces the known studies associated with resistance in above-mentioned conditions and SLIPS up to the present time. This review is followed in Chapter 3, by methods of manufacturing and characterisation of SLIPS. This chapter ends with a treatment protocol, which is used in all experiments.

Chapter 4 comprises the theoretical framework for all experiments. It provides calculation methods of the used quantities in the experiments for non-slip condition.

Chapter 5 deals with the experimental investigations in laboratory. Setup of rotating disc and rotating coaxial cylinders experiments are explained, and the results are shown. Statistical methods used in this study are included in this chapter.

Towing tank experiment setup is part of Chapter 6. This chapter includes choice of the ship model, towing test design and experimental results.

Conclusions and future research recommendations are the subject of the Chapter 7. This part gives unity to the entire study leading to the overall conclusions.

Chapter

2. Literature review

2. 1. Overview.

This chapter discusses current understanding of frictional resistance and methods for minimising it. The latter includes use of riblets, super-hydrophobic surfaces and lubricant infused surfaces.

Phenomena associated with drag reduction are studied and included in the review. These are slip and non-slip conditions, molecular interaction, wetting properties, and shear rate.

Methods of testing frictional resistance is another object of interest in this review. These methods comprise indirect and direct methods of measuring drag reduction.

2. 2. Boundary layers basics

Frictional resistance in ships is associated with the boundary layers concept. At laminar flows, for example, different layers of fluid move parallel to the wall/surface, with some velocity gradient outwards from the wall. These velocity gradient results in sheer forces usually denoted as surface or skin friction drag. The boundary layer in a turbulent flow is split into three layers. The layer closest to the wall is very thin and is called the viscous sub-layer. In that layer, viscosity forces are dominant. The next layer is called the buffer layer. This is where momentum and viscosity affect the flow in equal proportion. The outermost layer is momentum dominated and is called the outer layer or long layer

(Schetz, 1999). The viscous sublayer is the subject of interest where the solid-fluid interaction on a molecular level takes place and may affect total resistance.

2. 3. New technologies

Slippery Liquid Infused Porous Surface (SLIPS) was introduced by J. Aizenderg, a professor of chemistry and chemical biology at Harvard University, as an achievement of her lab. It is essential to explore SLIPS quality and potential ability to reduce drag, sometimes in combination with other techniques. There are indications that SLIPS might be suitable for drag reduction with the potential to also increase the resistance to biofouling (Bhushan, 2012; P. Kim, M. J. Kreder, J. Alvarenga, & J. Aizenberg, 2013a).

The reduction of skin friction at a microscopic level using new materials and production techniques is an area that has seen increasing research during the last decades and different approaches have been taken. One attempt to reduce surface drag is the use of so-called riblets. These are microscopic streamline fences with a height of 1-2% of the

boundary layer at low Reynolds number (M. Walsh & Weinstein, 1978; M. J. Walsh, 1980, 1982). These structures, sized between 10 µm to 150 µm, alter the boundary layer in a way that a reduction in drag up to 10% is achieved.

The initial work included a number of differently shaped riblets with varying height and spacing. It was found that the aspect ratio of height and space has a major effect on drag reduction (Bixler & Bhushan, 2013; Chen, Rao, Shang, Zhang, & Hagiwara, 2013). The original idea was adopted after observing similar but more complex microstructures that have been discovered on the surfaces/skins of living creatures, such as for example ridges and valleys on the scales of sharks. These microscopic structures significantly decrease skin frictional drag (Reif & Dinkelacker, 1982).

The method has been successfully adopted for aircraft wings (Bixler & Bhushan, 2013) and wind turbines blades (Chamorro, Arndt, & Sotiropoulos, 2013). Aquatic application however is associated with biofouling which can quickly erase the initial improvement. Bushan and Bixler (2013) expressed a possible link between the antifouling ability of marine creature's skin and the microstructure of riblets, but, so far, it not been experimentally verified. Their model did not include fish slime. So far limited studies have been done on artificial shark skin, impregnated with like substances (Jung & Bhushan, 2009; Wen, Weaver, & Lauder, 2014). Their ability to reduce drag and antifouling is still not well understood.

In general, it appears, contrary to the wide perception that the smoother the surface the less skin friction drag will occur, that roughness at a microscopic scale and in a specific style may decrease drag. Another area of research with potential applications to drag reduction is super hydrophobic surfaces, developing nano- and micro- patterns and

textures, creating, for example, air pockets. (Choi & Kim, 2006; Cecile Cottin-Bizonne, Barrat, Bocquet, & Charlaix, 2003; Muralidhar, 2011; Wu et al., 2014), see Figure 1a.

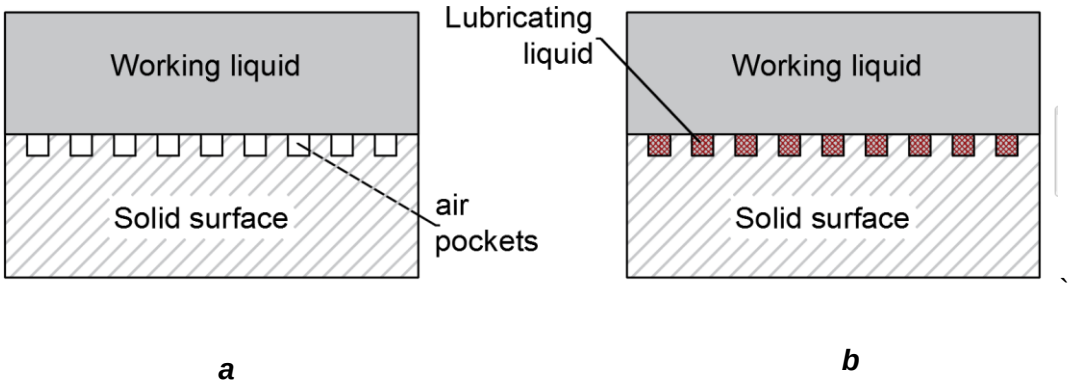

*Figure 1. Diagrammatic sketches of a surface with a nano/micro textured solid surface: (**a**) forming air pockets; (**b**) forming pockets filled with lubricated liquid (Smith et al., 2013)*

While riblets seem to be very effective at turbulent flow, super hydrophobic surfaces with entrapped air are more associated with drag reductions at laminar flow regimes, but have limited applications at higher turbulence (Rothstein, 2010).

Surfaces with air pockets are well studied and the effect of drag reduction is based on differences in the viscosities of water and air (Rothstein, 2010; Solomon, Khalil, & Varanasi, 2014). The biggest disadvantage of that specific approach for aquatic applications is the loss of air pockets due to an increase of outer pressure resulting in displacement of air by the liquid, (Lee & Kim, 2009).

In order to improve the stability of the lubricating substance, the entrapped air is best replaced with a liquid (Kim et al., 2013a; Quéré, 2005; Schönecker & Hardt, 2013). These types of surfaces, see Figure 1 b, can still be hydrophobic but are known as SLIPS or Lubricant Impregnated Surfaces. All these surfaces are topographically structured, having some sort of entrapped fluid lubricant, either gas or liquid.

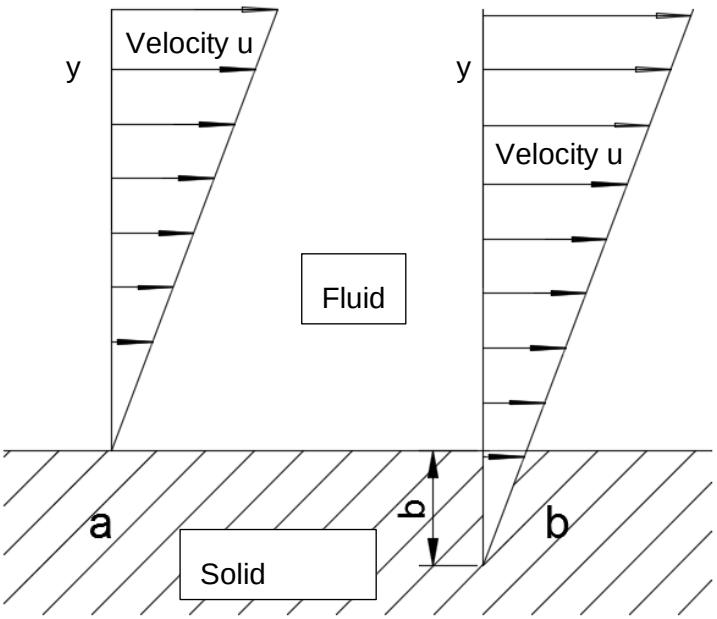

Figure 2. a. Nonslip condition at a boundary layer; b. Slip condition with slip length b. (Rothstein, 2010)

Drag reduction for these surfaces is associated with a slip condition at liquid-solid interface in the near wall boundary layer. It was first proposed by Navier in 1823 and can be expressed as the magnitude of the slip velocity, u_0, proportional to the shear rate, *du/dy*, where *y* expresses the coordinate direction normal to the surface. The proportion coefficient b depicts the slip length (Navier, 1823), see Figure 2.

$$u_0 = b \left|\frac{\partial u}{\partial y}\right| \qquad (1)$$

Maxwell (1879) worked on the slip length of gas flowing over solid surfaces and figured out that the slip length is of the order of the mean free path of the fluid. Later, however, it was found that the slip length is extremely small, about 1nm, and it may be neglected without loss of accuracy (Blake, 1990; Tolstoi, 1952). The consequence of that conclusion was that non-slip conditions were widely accepted for most normal flow conditions (Batchelor, 1985; Deen, 1998).

Nevertheless, ongoing research could experimentally identify slip for some specific cases with a liquid-solid interface. There are two classes of systems where slip affects the hydrodynamic behaviour of the flow. These are associated with either polymer melt (Priezjev & Troian, 2004, 2006), i.e. liquid state of thermoplastic polymers or simple liquid micro- and nano- flows. The latter is a subject of interest in this doctoral thesis.

The slip length varies from few nm to few hundreds of μm, as reported in numerous papers. For instance, a typical value of the slip length is in a range of 20 to 50 nm (Choi, Westin, & Breuer, 2003; Churaev, Sobolev, & Somov, 1984; C Cottin-Bizonne, Cross, Steinberger, & Charlaix, 2005; Horn, Vinogradova, Mackay, & Phan-Thien, 2000). However, the more significant slip length, one that may affect frictional resistance, is 1 to 50 μm (Choi & Kim, 2006; Schnell, 1956; Tretheway & Meinhart, 2002; Zhu & Granick, 2001). Finally, the most impressive values of slip length are between 100 and 400 μm (Lee & Kim, 2009; Watanabe, 1999).

The controlling parameters and the molecular origin of the phenomena have still not been completely agreed on between researchers (Priezjev & Troian, 2004). These may be either:

a) a weak molecular attraction between different phases (Blake, 1990; Tolstoi, 1952) or,

b) the shear rate exceeding the critical one (Thompson & Troian, 1997), i.e. slip length depends on a specific critical value of the shear rate. This critical value depends on the surface energy corrugation. The lower the corrugation, the lower the critical value of shear rate or,

c) wetting properties. Watanabe at al. argue that the wettability of the surface, measured in contact angle (see Figure 4) of a water drop governs the slip. If the contact angle is over 110°, slip will occur (Watanabe, 1999).

In an attempt to summarise the information about slip, two groups, molecular and apparent slip, are defined based on their origin (Lauga, Brenner, & Stone, 2007). Molecular slip may occur over a flat surface. It originates in a weak molecular interaction between the liquid and the surface, and the slip length is usually of the order of nanometres. Apparent slip is associated with greater slip lengths, and it occurs due to mixed no-slip and slip conditions over topographically structured surfaces. In case of gas being entrapped in the surface texture, the flowing liquid contacts the solid surface in a patchy manner.

While nano sized slip does not have a big effect on drag reduction, a larger slip, of order of micrometres is reported to have an effect of up to 70% of drag reduction in laboratory tests (Choi & Kim, 2006; Lee & Kim, 2009).

2. 4. Experimental investigations

Experimental methods for measuring slip can be split into two categories, indirect measuring, and direct measuring.

2. 4. 1. Indirect measuring of slip

For indirect measuring, the slip length is calculated using other measured variables like hydrodynamic forces or pressure drops. A pressure piping system or rheometer may be employed (Baudry, Charlaix, Tonck, & Mazuyer, 2001; Choi et al., 2003; C Cottin-Bizonne et al., 2005; Daniello, Waterhouse, & Rothstein, 2009; Jung & Bhushan, 2009; Schnell, 1956; Zhu & Granick, 2001).

A pressure piping system consists of pipe work providing constant full-bore flow to the testing pipe. The interior of the testing pipe is treated according to the experimental surface texture or coating. Pressure gauges are installed at both ends of the testing pipe. According to fluid mechanics, a pressure drop will occur due to friction. In the case of slip, the pressure drop will be small compared to the pressure drop inside the controlled pipe.

Rheometers may be of varying designs. Generally, they measure flows of fluids under an applied force. Often ‘cone and plate’ is used in these tests and the torque required for rotation of the cone is measured. The plate forms the experimental surface to be tested.

2. 4. 2. Direct measuring of slip

Direct measurement is difficult and involves more complex equipment such as Micro-Particle Image Velocimetry (VIP) or Total Internal Reflection Fluorescence Microscopy IRFM) (Daniello et al., 2009; Jin, Huang, Park, Yoo, & Breuer, 2004; Joly, Ybert, &

Bocquet, 2006; Joseph & Tabeling, 2005; Park, Sun, & Kim, 2014; Peguero & Breuer, 2009; Pit, Hervet, & Léger, 1999; Woolford, Prince, Maynes, & Webb, 2009).

2. 4. 3. Numerical simulation for predicting slip

Alternative approaches for investigating the slip length, are either purely theoretical or by using numerical simulations. Numerical simulation methods can produce important predictions and a very detailed insight but do require experimental verification. The initial assumption regarding a mathematical model was that the flow past super-hydrophobic surfaces is shear-free at the water-air interface and that this interface is flat (Cécile Cottin-Bizonne, Barentin, Charlaix, Bocquet, & Barrat, 2004; Lauga & Stone, 2003). Later work introduced mixed boundary conditions, non-slip over solid surfaces and slip over air-entrapped pockets. From thee considered model, it appears that the drag reduction depends on the fraction of the shear-free area as well as on the dimensionless channel depth or radius. Slip length is also a function of the dimensional period of the roughness. Both these are geometric characteristics of texturing. Scaling analysis contributed to refining the model but the assumptions remained the same (Ybert, Barentin, Cottin-Bizonne, Joseph, & Bocquet, 2007). The results were verified by experiments with vanishingly small solid fractions (Lee, Choi, & Kim, 2008). This model however is limited to gases being the second lubricant-impregnating fluid. When it comes to microscopically different topographical surface geometries, the viscosities of the fluid filling the cavities and the fluid in the main flow will affect the slippage (Busse, Sandham, McHale, & Newton, 2013; Schönecker, Baier, & Hardt, 2014). Schönecker and Hardt (2015) analysed arbitrary combinations of Newtonian fluids in both situations filling the indentations and flowing over the surface. They define a threshold for the occurrence of drag reduction for flows in a channel or in a tube.

2. 4. 4. Direct observations

In close observations, using an atomic force microscope (Zhu & Granick, 2001), neutron scattering experiments (Doshi, Watkins, Israelachvili, & Majewski, 2005) and x-ray scattering (Migler, Hervet, & Leger, 1993), it is found that not only a carpet of nano-bubbles and/or gaps cover the surface of super hydrophobic surface but the water structure has also shifted, lowering the density (Chandler, 2007). The latter may be expressed as a two-layer system flow near the hydrophobic surface: one layer called bulk with density μ_{bulk} and a thin microscopic layer with δ thickness and density μ_{wall} (Berg, Cense, Hofman, & Smits, 2008; Bunkin et al., 1997; Vinogradova, 1995), see Figure 3. Choi and Kim (2006) expressed the slip length as:

$$b = \delta\left(\frac{\mu_{bulk}}{\mu_{wall}} - 1\right) \qquad (2)$$

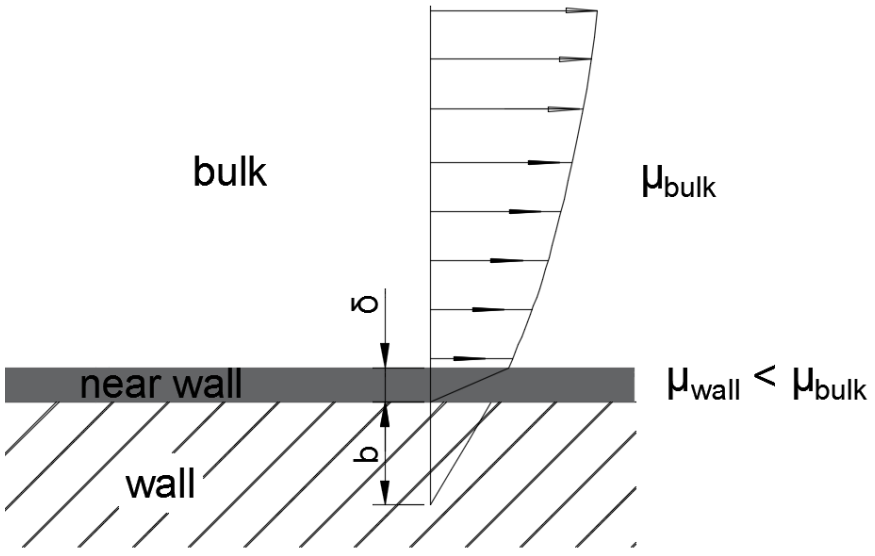

Figure 3. Change of the viscosity of the water at the near wall layer (Berg et al., 2008)

Whilst the above-mentioned phenomena are observed for air as a second impregnating fluid, no information was found for the effect of other impregnating fluids.

2. 5. Substrates and lubricants for SLIPS

In the process of designing slippery surfaces, the choice of materials is critical. Typical substrates used in recent studies are limited to silicon wafer which is chosen for its low surface energy (Smith et al., 2013; Solomon et al., 2014). Smith et al. (2013) used lithographically patterned silicon micro-post arrays; another nano-structured silicon. They noted the importance of wetting ability of the impregnating lubricant over the substrate.

The wetting ability is often defined by the contact angle of a drop over the surface, see Figure 4. It may be measured using a contact angle telescope-goniometer. This device uses an optical system to capture how a liquid droplet sits on the solid surface. Using a high definition digital camera installed in the device and corresponding imaging software, the contact angle can be measured; see Figure 4. It is one of the popular methods in defining wetting properties of liquids over surfaces (Israelachvili, 1992; Yuan & Lee, 2013).

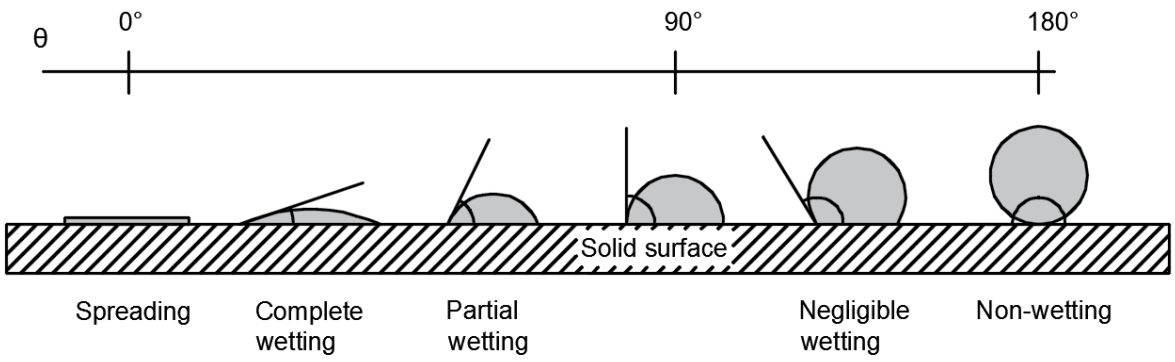

Figure 4. Contact angle of a drop over wetting to non-wetting surface (Majeed, 2014)

If the contact angle of a lubricant over a flat surface of substrate is zero, it will most likely establish a very thin film/layer. In case of a contact angles greater than zero, it is likely that the posts, geometrical features of nano-textured surface, will not be covered after the impregnating process. This alters the conditions for slip due to a change in the surface patching pattern, wetted and not wetted (Smith et al., 2013; Solomon et al., 2014).

Ünal, Ünal, & Atlar *(2012)* give the following formula for the critical contact angles for impregnation, θ_c

$$\theta_c = cos^{-1}\left[\frac{(1-\phi_s)}{(r-\phi_s)}\right] \quad (3)$$

where *r* is the ratio of the total surface area of the textured surface to its projected area and ϕ_s is the fraction of the projected area of the textured surface that is occupied by a solid, i.e. the solid fraction (Quéré, 2005; Solomon et al., 2014).

Solomon at al. (2014) established a relation between drag reduction and the viscosity ratios of working and lubricating liquids. After studying arbitrary liquids for both applications, working or lubricating liquids, it was found that, for laminar flow, drag reduction is the higher the greater the ratio between viscosity of the working liquid and the viscosity of lubricating liquid.

However, turbulent flow has not been experimentally thoroughly studied. Recently some theoretical models have been developed. Schönecker and Hardt (2015) have showed that not all slippery surfaces are capable of drag reduction at turbulent flow. For instance, if the viscosity of the lubricating liquid is relatively high then a reduction in drag may not occur and the drag may even increase.

The stability of the lubricant impregnated surface however is considered by means of the capillary forces arising from the microscopic texture. Possible evaporation or wash out by droplets rolling over such surfaces are mentioned by Smith et al. (2013) and Solomon et al. (2014) but are not studied in depth. However, the effect of wash out is of major concern for aquatic applications and it is not studied.

The research associated with lubricant infused surfaces are often linked to micro-fluids or polymer flow. Many types of fluids are involved in that regards and typical substrate is silicon wafer. Marine application, however, is not studied. In this case, the working fluid is water fresh, or sea and the substrate depends on the type of marine vehicle. This study explores SLIPS designed for aluminium surfaces since many marine vehicles are built using this material and working fluid is water.

Chapter

3. Surface manufacturing and characterisation

3. 1. Introduction

The exploration of the potential for drag reduction of SLIPS begins with the production of such surfaces and their characterisation. The manufacturing of tested specimens is based on aluminium alloy substrate with the surface anodised. Anodising is the process in which a certain porosity of the surface is achieved. In order to characterise pores on the surface, the Scan Electron Microscope (SEM) at Auckland University of Technology was used. Further, silicon oil was used to saturate the porous surface shortly after anodising. The same treatment was applied for all three sets of experiments.

3. 2. Creating Slippery Lubricant Infused Porous Surface

3. 2. 1. Choice of substrate

Due to the aquatic environment, corrosion resistance is a major concern. Aluminium exhibits excellent anti corrosion properties in water and therefore aluminium alloys are popular in marine applications. Kim et al. (2013) used it as a substrate. It is possible to apply an aluminium coating and create a thin layer over any other base.

An alternative option is a silicon film. Silicon was used by Smith et al. (2013) and their choice was based on its low surface energy. The latter helps to establish a water repellent ability, which is desirable for this application. Additionally, silicon in a form of coating may provide corrosion protection and a base for polymer grafting.

Polymer grafting is a technique that allows long chain molecules to attach to the main polymer structure. It is possible that the attached long molecules to act as mini riblets, (Sherazi, 2016). However, this technique has not yet been investigated for drag reduction.

Due to the complexity and chemical challenges of the above-mentioned silicon film technique, aluminium alloy substrate was chosen.

3. 2. 2. Treatment

The treatment for SLIPS was suggested in “Hierarchical or Not? Effect of the Length Scale and Hierarchy of the Surface Roughness on Omniphobicity of Lubricant-Infused Substrates” (Kim et al., 2013a). It explores the idea of creating a surface with pores filled with a lubricant. Philseok Kim provided the protocols he and his team used for attempting to achieve SLIPS in their research.

Kim’s SLIPS is built on an aluminium base. Initially the surface is micro structured by sandblasting. Nano-structuring happens by producing boehmite, which is Aluminium Oxide Hydroxide that naturally occurs in some aluminium ores. Kim suggests a process of boiling cleaned sandblasted surfaces of aluminium alloy in order to achieve the desired nano-structuring.

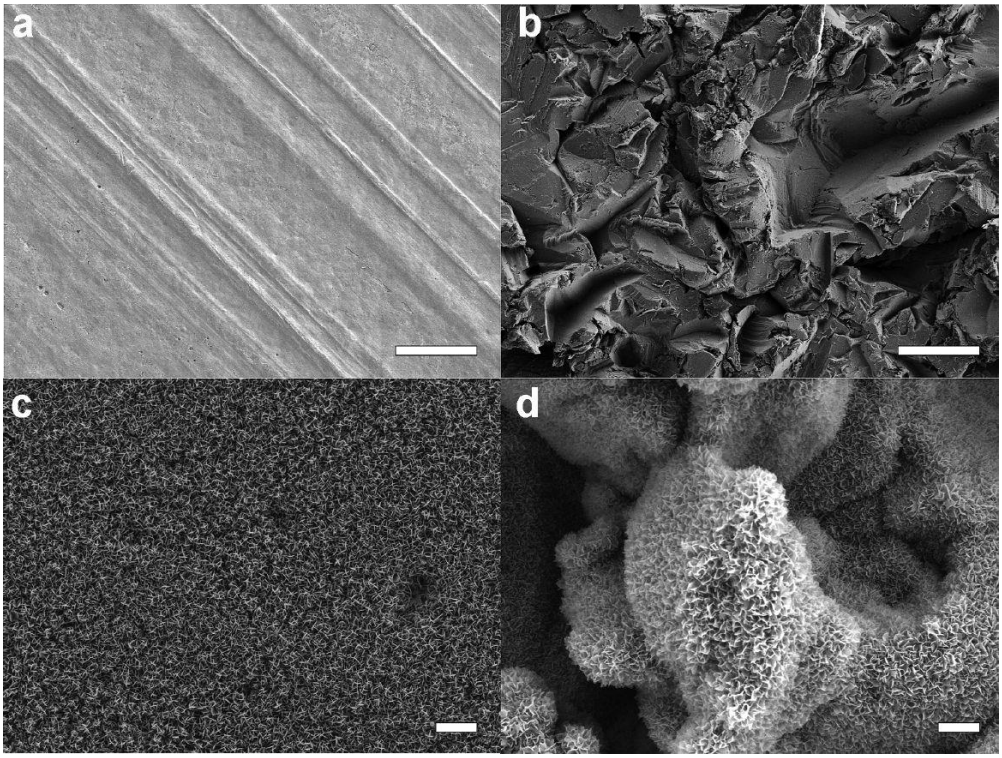

Figure 5. SEM (Scanning Electron Microscope) images of the surface topography of: (a) untreated aluminium, (b) sandblasted micro-structured aluminium, (c) nanoscale boehmite on flat aluminium, (d) hierarchical texture of sandblasted and boehmitised aluminium. Scale bars are 50 μm for (a, b) and 1 μm for (c, d). (Kim et al., 2013a).

The required chemicals for producing SLIPS were also identified using the provided protocols. However, it was noticed that some of these chemicals are included in the list of Persistent Organic Pollutants (POPs), according to the Stockholm convention of 1997, ("Stockholm Convention,"). Persistent pollutants do not decompose over time but accumulate in nature and are therefore not sustainable. Chemicals of this category, as found in Kim's study, are Perfluorooctane sulfonic acid and perfluorooctane sulfonyl fluoride. They are included in annex B of the Stockholm convention – 'use with restrictions'.

Nevertheless, they are required for fluorination of the already nano-porous surfaces in order for the perfluoropolyether (PFPE) lubricant to adhere to that surface. While lubricants of that sort are available on the market, sulfonic acid has to be synthesised.

It was decided therefore to try alternative methods avoiding environmentally unfriendly chemicals.

3. 2. 3. Specimen surface structuring

The specimens were prepared at Unitec, Auckland. Aluminium alloy 5005 H32 was used to prepare pieces measuring 50 x 20 x 3 mm. The choice of the material was based on the fact that it is commonly used in marine applications and is readily available. Some of the pieces were sandblasted with sand at 100 psi (690kPa). The largest measured particles were 0.5 mm relating to grit 40. The roughness was determined in AUT's laboratory, using a Taylor Hobson roughness reader at 0.5 m/s. The results are presented on Table 1. This shows that the sandblasting produced a rougher surface compared to the surface prescribed by Kim et al. (2013).

Table 1. Measured surface roughness of the specimen.

	Ra (arithmetical mean) µm	*Rz* (ten-point mean) µm
Original surface	0.24	3
Sandblasted surface	3.4	27.4

Nano-structuring was carried out at Unitec's lab. Specimens were sanded under water using sandpaper grit 280 in order to remove any aluminium oxides from the surface. Next, they were cleaned in acetone by brushing and rinsing. After air-drying, the specimens were submerged in boiling water (100°C) for 10, 30, 60, 90 and 120 minutes.

A Raman confocal microscope was used for initial observations. It showed the presence of Boehmite. However, the layer was extremely thin, and it was assumed that it would not be useful as an absorbent. The sandblasted specimens had spots without boehmite at all. A possible reason was that the aluminium specimen should have been boiled immediately after sandblasting, otherwise natural oxides are formed on the surface instead of hydroxides. It was impossible to combine both facilities in immediate proximity and that was the reason to look for alternative solution.

3. 2. 4. Improvements

Anodising is an alternative method for creating porous surfaces. To explore this, six specimens similar to the previous attempt were prepared, i.e., 50 x 20 x 3 mm made of Aluminium alloy 5005 H32. The anodising was done commercially.

This technique meets the principles of SLIPS initial steps for fabrication (Kim et al., 2013a), i.e. the surface was firstly micro textured and then nano structured. This was done by *Anodising Industries Limited*, based in Onehunga, Auckland, New Zealand.

Anodising is an electro-chemical process, leading to a build-up of a layer of aluminium oxide organized in a honeycomb structure, forming pores, see Figure 6. Pore sizes are usually 10-150 nm in diameter (Edwards, 1997), although the actual size in this study is of order of 10-20 µm.

The final step in the process is to protect aluminium from further oxidation; the pores are sealed by boiling or steaming. The latter process produces a layer of nano-sized boehmite structure. The thickness of the anodised surface layer is 10 to 12 µm, as stated by the manufacturer.

According to the commercial designation, this is type 2 class 1. US Military Specification MIL-A-8625 gives some details about this classification. Type 2 uses sulphuric Acid and class 1 designates an undyed finish, i.e. clear (Osborn, 2014).

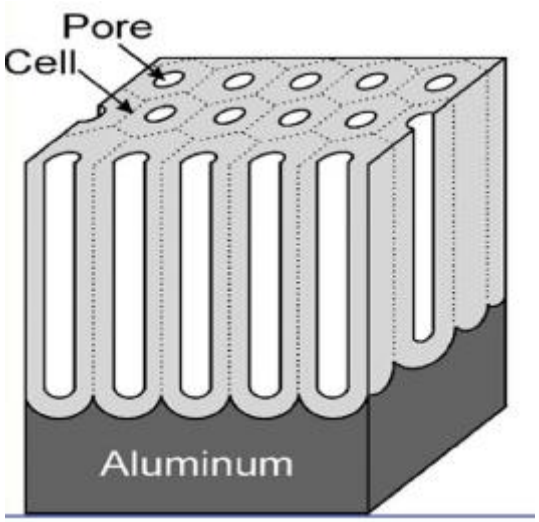

Figure 6. Aluminium oxide cells formed due to anodising process over aluminium. Adopted from *www.hobbychemicals.com.au*

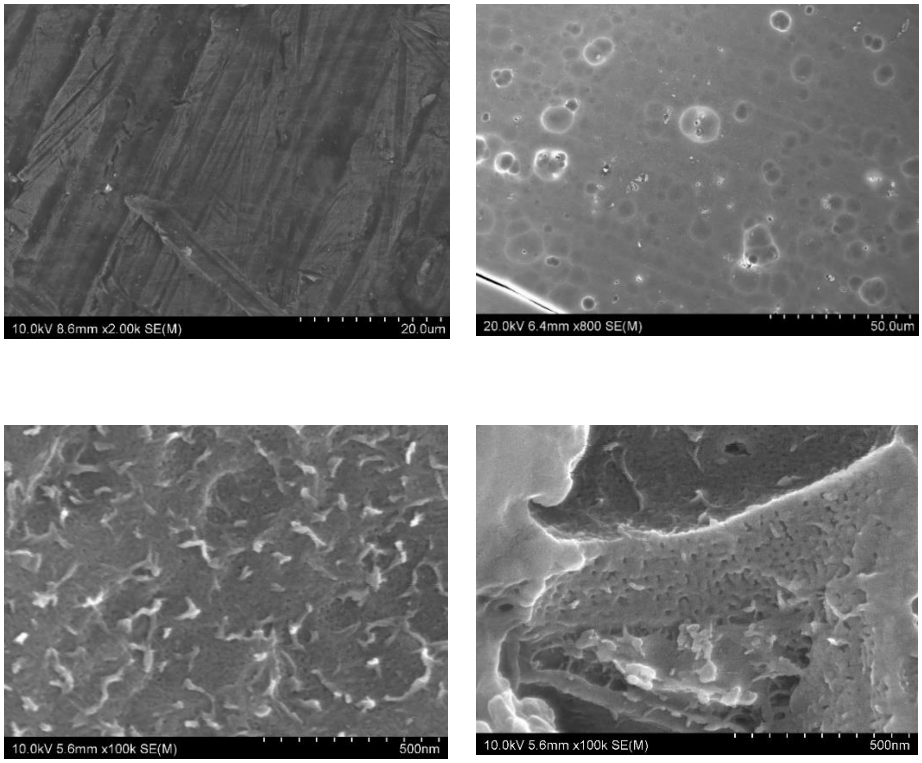

Figure 7. SEM images of the surface topography of: (a) untreated aluminium, scale bars are 20 µm, (b) anodised aluminium, scale bars are 50 µm, (c) nanoscale boehmite on flat aluminium, (d) anodised and boehmitised aluminium. Scale bars are 500 nm for (c, d).

Small samples of the anodised and boehmited aluminium were characterised using the Scanning Electron Microscope (SEM) at AUT before applying lubricant. Figure 7 contains four images. Image (a) shows the untreated aluminium surface. The scale bar there is 20 µm; Image (b) shows a hexagon pattern of the surface. The scale bar is 50 µm, so the size between the hexagons can be identified to be within a range from 10 to 20 µm. Images (c) and (d) have scale bar of 500 nm. These show much a finer structure of boehmite.

3. 2. 5. Infusion

Choice of lubricant.

The choice of lubricating liquid is governed by two factors: how it spreads over the substrate and what is the water's behaviour along the lubricating liquid. Smith et al. (2013) chose silicon oil and trifluoromethylsulfonyl based on these criteria.

Silicon oil was chosen for its hydrophobic and lubricating properties. The form of silicon used was Dot 5 brake fluid. According to the Material Safety Data Sheet of DOT-5 Silicone Brake Fluid, it contains 95% Polydimethylsiloxane, which is known as silicon oil.

The specimens were soaked in the oil and wiped out by soft cloth. It was noted that if not effectively wiped and a shiny surface revealed itself, the drag reduction did not occur because an additional heavy film formed.

Heated surfaces or oil did not affect the outcome when tested for drag reduction.

3. 3. Treatment protocol

A treatment protocol was established for all experimental work. The tested surfaces are to be commercially anodized marine grade, which means the thickness of the layer is 25 μm. Natural close cell finish provides nano-structured surface without any additives i.e., pure boehmite seal. The next step is to apply Dot 5 brake fluid using a brush. Thorough whipping with soft cloth is critical end of the procedure. The surface has to be shiny without any apparent film left.

In this work, the surface treated in above mentioned, manner is called “treated”. The control surfaces, flat or cylindrical, are “non-treated”. It means that they are left as

manufactured. An example of the roughness of such surface is given in Table 1, called original surface.

Chapter

4. Theoretical Formulation

4.1. Introduction

The quantity of interest in this study is force and torque which are measured and/or calculated. These are defined as an integral of a stress over an area and for torque arm is involved as well. To determine an integral, the integrand must be known. That is why fluid mechanics description of the flow is included.

The theoretical framework of this study is divided in three parts including rotating disk, rotating coaxial cylinders and ships theory. Each part contains equations describing the fluid flow in the specified conditions. These equations are developed for no slip conditions. Formulation of torque and/or forces are included.

4. 2. Governing equations for a flow

Fluid flow is described by the so-called Navier-Stokes equations and continuity equation. These equations are based on an assumption that the flow is laminar and shear rate linearly relates to shear stress in the fluid. The equations can be used for turbulent flow after some modifications. (Peter R.N Childs, 2011)

These equations are developed using Cartesian coordinate system and a fluid element is considered, see Figure 8.

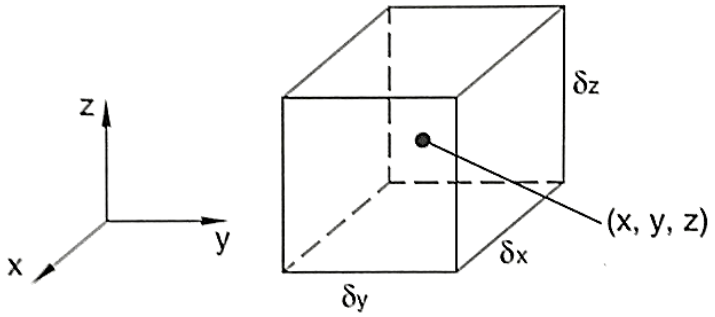

Figure 8. Cartesian coordinate system and fluid element(Peter R. N. Childs, 2011)

The forces acting on this element are surface forces, body forces and inertia forces. Formulation of the system of equations expresses dynamic balance between all these forces, (Peter R.N Childs, 2011). Each equation is written for one of the three directions *x*, *y* and *z*.

Let consider direction *x*.

Inertia forces are expressed by following mathematical expression

$$\rho\left(\frac{\partial u_x}{\partial t}+u_x\frac{\partial u_x}{\partial x}+u_y\frac{\partial u_x}{\partial y}+u_z\frac{\partial u_x}{\partial z}\right)=Inertia\ forces$$

Where ρ is density of the fluid, *t* is time, u_x represents velocity in in direction x.

Surface forces are resulting from shear and normal stresses. These forces are viscosity μ dependant and mathematically are expressed by viscose term and pressure term. Viscose term in *x* direction is

$$-\frac{2}{3}\frac{\partial}{\partial x}\left[\mu\left(\frac{\partial u_x}{\partial x}+\frac{\partial u_y}{\partial y}+\frac{\partial u_z}{\partial z}\right)\right]+2\frac{\partial}{\partial x}\left(\mu\frac{\partial u_x}{\partial x}\right)+\frac{\partial}{\partial y}\left[\mu\left(\frac{\partial u_x}{\partial y}+\frac{\partial u_y}{\partial x}\right)\right]+\frac{\partial}{\partial z}\left[\mu\left(\frac{\partial u_x}{\partial z}+\frac{\partial u_z}{\partial x}\right)\right]$$

$$=Viscosity\ dependand\ component\ of\ forces\ i.e.visdose\ term$$

Pressure term in *x* direction is $\frac{\partial p}{\partial x}$, where p is pressure,

Body forces in *x* direction are expressed by $\mathrm{F_x}$

The resultant equation for *x* direction when inertia forces balance the surface and body forces becomes

$$\rho\left(\frac{\partial u_x}{\partial t}+u_x\frac{\partial u_x}{\partial x}+u_y\frac{\partial u_x}{\partial y}+u_z\frac{\partial u_x}{\partial z}\right)=-\frac{\partial p}{\partial x}-\frac{2}{3}\frac{\partial}{\partial x}\left[\mu\left(\frac{\partial u_x}{\partial x}+\frac{\partial u_y}{\partial y}+\frac{\partial u_z}{\partial z}\right)\right]+ 2\frac{\partial}{\partial \mathrm{x}}\left(\mu\frac{\partial \mathrm{u_x}}{\partial \mathrm{x}}\right)+\frac{\partial}{\partial \mathrm{y}}\left[\mu\left(\frac{\partial \mathrm{u_x}}{\partial \mathrm{y}}+\frac{\partial \mathrm{u_y}}{\partial \mathrm{x}}\right)\right]+\frac{\partial}{\partial \mathrm{z}}\left[\mu\left(\frac{\partial \mathrm{u_x}}{\partial \mathrm{z}}+\frac{\partial \mathrm{u_z}}{\partial \mathrm{x}}\right)\right]+\mathrm{F_x} \quad (4)$$

Following similar flow of thoughts for *y* and *z* directions the flow motion equations for these directions are:

$$\rho\left(\frac{\partial u_y}{\partial t}+u_x\frac{\partial u_y}{\partial x}+u_y\frac{\partial u_y}{\partial y}+u_z\frac{\partial u_y}{\partial z}\right)=-\frac{\partial p}{\partial y}-\frac{2}{3}\frac{\partial}{\partial y}\left[\mu\left(\frac{\partial u_x}{\partial x}+\frac{\partial u_y}{\partial y}+\frac{\partial u_z}{\partial z}\right)\right]+ 2\frac{\partial}{\partial \mathrm{y}}\left(\mu\frac{\partial \mathrm{u_y}}{\partial \mathrm{y}}\right)+\frac{\partial}{\partial \mathrm{x}}\left[\mu\left(\frac{\partial \mathrm{u_x}}{\partial \mathrm{y}}+\frac{\partial \mathrm{u_y}}{\partial \mathrm{x}}\right)\right]+\frac{\partial}{\partial \mathrm{z}}\left[\mu\left(\frac{\partial \mathrm{y}}{\partial \mathrm{z}}+\frac{\partial \mathrm{u_z}}{\partial \mathrm{y}}\right)\right]+\mathrm{F_y} \quad (5)$$

and

$$\rho\left(\frac{\partial u_z}{\partial t}+u_x\frac{\partial u_z}{\partial x}+u_y\frac{\partial z}{\partial y}+u_z\frac{\partial u_z}{\partial z}\right)=-\frac{\partial p}{\partial z}-\frac{2}{3}\frac{\partial}{\partial z}\left[\mu\left(\frac{\partial u_x}{\partial x}+\frac{\partial u_y}{\partial y}+\frac{\partial u_z}{\partial z}\right)\right]+ 2\frac{\partial}{\partial z}\left(\mu\frac{\partial u_z}{\partial z}\right)+\frac{\partial}{\partial x}\left[\mu\left(\frac{\partial u_x}{\partial z}+\frac{\partial z}{\partial x}\right)\right]+\frac{\partial}{\partial y}\left[\mu\left(\frac{\partial y}{\partial z}+\frac{\partial u_z}{\partial y}\right)\right]+F_z \quad (6)$$

Considering water, as in this study, viscosity and density are assumed constant at a specific temperature, which significantly simplifies the system of equations. Hence, equations (4), (5) and (6) are converted to the following:

$$\rho\left(\frac{\partial u_x}{\partial t}+u_x\frac{\partial u_x}{\partial x}+u_y\frac{\partial u_x}{\partial y}+u_z\frac{\partial u_x}{\partial z}\right)=-\frac{\partial p}{\partial x}+\mu\left(\frac{\partial^2 u_x}{\partial x^2}+\frac{\partial^2 u_x}{\partial y^2}+\frac{\partial^2 u_x}{\partial z^2}\right)+F_x \quad (7)$$

$$\rho\left(\frac{\partial \mathrm{u_y}}{\partial \mathrm{t}}+\mathrm{u_x}\frac{\partial \mathrm{u_y}}{\partial \mathrm{x}}+\mathrm{u_y}\frac{\partial \mathrm{u_y}}{\partial \mathrm{y}}+\mathrm{u_z}\frac{\partial \mathrm{u_y}}{\partial \mathrm{z}}\right)=-\frac{\partial \mathrm{p}}{\partial \mathrm{y}}+\mu\left(\frac{\partial^2 \mathrm{u_y}}{\partial \mathrm{x}^2}+\frac{\partial^2 \mathrm{u_y}}{\partial \mathrm{y}^2}+\frac{\partial^2 \mathrm{u_y}}{\partial \mathrm{z}^2}\right)+\mathrm{F_y} \quad (8)$$

$$\rho\left(\frac{\partial u_z}{\partial t}+u_x\frac{\partial u_z}{\partial x}+u_y\frac{\partial z}{\partial y}+u_z\frac{\partial u_z}{\partial z}\right)=-\frac{\partial p}{\partial z}+\mu\left(\frac{\partial^2 u_z}{\partial x^2}+\frac{\partial^2 u_z}{\partial y^2}+\frac{\partial^2 u_z}{\partial z^2}\right)+F_z \quad (9)$$

4. 3. Rotating disks

4. 3. 1. Governing equations for a flow over a free disk

When describing rotating flow, it is convenient to use cylindrical, polar coordinates rather than Cartesian (see Figure 9 for definition). For the transformation between the two coordinate systems, following equations are used:

$$\mathrm{x}=\mathrm{r}\cos\varphi \quad (10)$$

$$\mathrm{y}=\mathrm{r}\sin\varphi \quad (11)$$

$$\mathrm{z}=\mathrm{z} \quad (12)$$

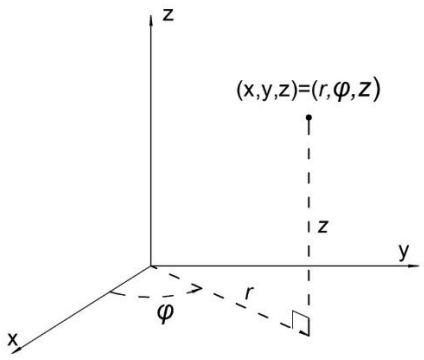

Figure 9. Cylindrical coordinate system

After substitution and rearrangement equations (7), (8) and (9) become

$$\rho\left(\frac{\partial u_r}{\partial t}+u_r\frac{\partial u_r}{\partial r}+\frac{u_\varphi}{r}\frac{\partial u_r}{\partial \varphi}+u_z\frac{\partial u_r}{\partial z}-\frac{u_\varphi^2}{r}\right)=-\frac{\partial p}{\partial r}+\mu\left(\frac{\partial^2 \mathrm{u_r}}{\partial \mathrm{r}^2}+\frac{1}{\mathrm{r}}\frac{\partial \mathrm{u_r}}{\partial \mathrm{r}}-\frac{\mathrm{u_r}}{\mathrm{r}^2}+\frac{1}{\mathrm{r}^2}\frac{\partial^2 \mathrm{u_r}}{\partial \varphi^2}+\frac{\partial^2 \mathrm{u_r}}{\partial \mathrm{z}^2}-\frac{2}{\mathrm{r}^2}\frac{\partial \mathrm{u}_\varphi}{\partial \varphi}\right)+\mathrm{F_r} \quad (13)$$

$$\rho\left(\frac{\partial u_\varphi}{\partial t}+u_r\frac{\partial u_\varphi}{\partial r}+\frac{u_\varphi u_r}{r}+\frac{u_\varphi}{r}\frac{\partial u_\varphi}{\partial \varphi}+u_z\frac{\partial u_\varphi}{\partial z}\right)=-\frac{1}{r}\frac{\partial p}{\partial \varphi}+\mu\left(\frac{\partial^2 \mathrm{u}_\varphi}{\partial \mathrm{r}^2}+\frac{1}{\mathrm{r}}\frac{\partial \mathrm{u}_\varphi}{\partial \mathrm{r}}-\frac{\mathrm{u}_\varphi}{\mathrm{r}^2}+\frac{1}{\mathrm{r}^2}\frac{\partial^2 \mathrm{u}_\varphi}{\partial \varphi^2}+\frac{\partial^2 \mathrm{u}_\varphi}{\partial \mathrm{z}^2}+\frac{2}{\mathrm{r}^2}\frac{\partial \mathrm{u_r}}{\partial \varphi}\right)+\mathrm{F}_\varphi \quad (14)$$

$$\rho\left(\frac{\partial u_z}{\partial t}+u_r\frac{\partial u_z}{\partial r}+\frac{u_\varphi}{r}\frac{\partial u_z}{\partial \varphi}+u_z\frac{\partial u_z}{\partial z}\right)=-\frac{\partial p}{\partial z}+\mu\left(\frac{\partial^2 \mathrm{u_z}}{\partial \mathrm{r}^2}+\frac{1}{\mathrm{r}}\frac{\partial \mathrm{u_z}}{\partial \mathrm{r}}+\frac{1}{\mathrm{r}^2}\frac{\partial^2 \mathrm{u_z}}{\partial \varphi^2}+\frac{\partial^2 \mathrm{u_z}}{\partial \mathrm{z}^2}\right)+\mathrm{F_z} \quad (15)$$

A free rotating disk is defined as a single disk that rotates in an initially stationary fluid. The disk radius is *b* and the angular velocity about *z*-axis is Ω, see Figure 10.

Once the disk is set in motion, a boundary layer δ will develop on each side of the disk. Figure 10 shows one side. At non-slip conditions, fluid particles will have the same

tangential velocity u_φ as the disk at distance r from the centre of rotation i.e., $u_\varphi = \Omega r$. When considering the distance along axis z, at $z \geq \delta$ $u_\varphi = 0$.

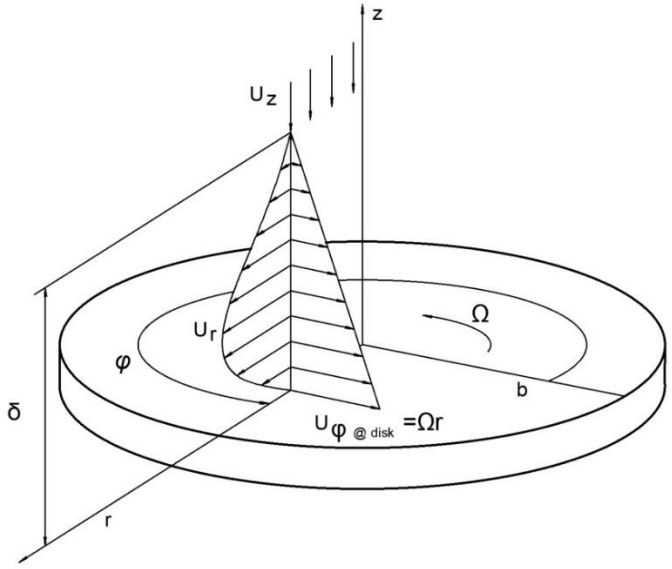

Figure 10. Rotating disc with radius b, angular velocity Ω, radial flow velocity u_r, tangential flow velocity u_φ and axial flow velocity u_z within boundary layer δ. (Peter R.N Childs, 2011)

On the other hand, rotational motion will develop centrifugal forces and thus radial flow. The radial velocity component will be zero at the disc and it will also be zero at free stream i.e., when $z \geq \delta$.

Due to conservation of mass and the presence of outflow, axial inflow will develop and will compensate the displaced mass of fluid particles. The axial velocity component is denoted u_z.

The flow regime, laminar or turbulent, within boundary layer depends on angular velocity and distance from the centre of rotation. This is due to the ratio of relative magnitude of inertia to viscous effects expressed by the local rotational Reynolds number $Re_{\varphi,\ local}$, see equation (16).

$$Re_{\varphi,\ local} = x^2 Re_{\varphi} = \left(\frac{r}{b}\right)^2 \frac{\rho \Omega b^2}{\mu} = \frac{\rho \Omega r^2}{\mu} \quad (16)$$

where *x* is the ration of the local radius, *r*, and *b* is the disc outer radius (Peter R.N Childs, 2011).

4. 3. 2. Laminar flow over a free disk

In order to analyse the behaviour of a fluid, a Eulerian approach is taken which means that, for a fixed location in space, the motion of a given fluid is understood. The Navier-Stokes and the continuity equations give a sufficient description of that motion. When adding a specific condition and analysis strategy, these equations may be transformed to a set of ordinary differential equations and be solved numerically or by other means. This was investigated by von Karman and later by Cochran (Cochran, 1934; Karman, 1921).

As described earlier, a cylindrical coordinate system is convenient for the definition of flow over a rotating disk. The origin of this system is the centre of the disk. Each point of the flow is described by the distance from the centre along its radius, *r*, azimuthal angle, *φ,* and distance along the axis of rotation, *z*, (see Figure 9).

Consequently, the continuity equation in cylindrical coordinates is

$$\frac{\partial u_r}{\partial r} + \frac{u_r}{r} + \frac{1}{r}\frac{\partial u_\varphi}{\partial \varphi} + \frac{\partial u_z}{\partial z} = 0, \quad (17)$$

Considering laminar flow conditions, the continuity equation (17) and Navier-Stokes equations (13) to (15) can be simplified. If indeed the flow is steady and symmetrical, the velocity elemental change with time and azimuth angle is negligible. Another important point is that some terms, such as $\frac{u_r}{r^2}$ and $\frac{u_\varphi}{r^2}$, are significantly smaller than other viscous terms and can be ignored. Finally, it may be assumed that body forces are negligibly small and can also be ignored. (Peter R.N Childs, 2011)

The simplified continuity equation and Navier-Stokes equations become:

$$\frac{\partial u_r}{\partial r} + \frac{u_r}{r} + \frac{\partial u_z}{\partial z} = 0 \qquad (18)$$

$$\rho\left(u_r \frac{\partial u_r}{\partial r} + u_z \frac{\partial u_r}{\partial z} - \frac{u_\varphi^2}{r}\right) = -\frac{\partial p}{\partial r} + \mu\left(\frac{\partial^2 u_r}{\partial r^2} + \frac{1}{r}\frac{\partial u_r}{\partial r} + \frac{\partial^2 u_r}{\partial z^2}\right) \qquad (19)$$

$$\rho\left(u_r \frac{\partial u_\varphi}{\partial r} + \frac{u_\varphi u_r}{r} + u_z \frac{\partial u_\varphi}{\partial z}\right) = -\frac{1}{r}\frac{\partial p}{\partial \varphi} + \mu\left(\frac{\partial^2 \varphi}{\partial r^2} + \frac{1}{r}\frac{\partial u_\varphi}{\partial r} + \frac{\partial^2 u_\varphi}{\partial z^2}\right) \qquad (20)$$

$$\rho\left(u_r \frac{\partial u_z}{\partial r} + u_z \frac{\partial u_z}{\partial z}\right) = -\frac{\partial p}{\partial z} + \mu\left(\frac{\partial^2 u_z}{\partial r^2} + \frac{1}{r}\frac{\partial u_z}{\partial r} + \frac{\partial^2 u_z}{\partial z^2}\right) \qquad (21)$$

For boundary non-slip conditions where z is greater than zero and r is less than the disc radius b, at disc surface it may be stated that:

when $z = 0$

$$\left.\begin{array}{l} u_z = 0 \\ u_\varphi = r\Omega \\ u_r = 0 \end{array}\right| \qquad (22)$$

and when z approaches ∞

$$u_\varphi = 0 \qquad u_r = 0 \qquad (23)$$

A solution to equations (18) to (21) will give full information of the behaviour of particles of the fluid for any location. This solution, however, will depend on the specific values of the rotational speed, viscosity, and density. A universal approach is to transform this set of equations, so they become dimensionless. The following transformations are used in the process:

$$z_* = z \sqrt{\frac{\Omega}{\nu}} \qquad (24)$$

$$u_{r*}(z_*) = \frac{u_r}{r\Omega} \qquad (25)$$

$$u_{\varphi*}(z_*) = \frac{u_\varphi}{r\Omega} \qquad (26)$$

$$u_{z*}(z_*) = \frac{u_z}{\sqrt{\nu\Omega}} \qquad (27)$$

$$p_*(z_*) = -\frac{p}{\mu\Omega} = -\frac{p}{\rho\nu\Omega} \qquad (28)$$

The asterisk (*) sign indicates these are dimensionless variables, and brackets on the left side of the equations signify that the variable is a function of a dimensionless axial

location z_*. After substitution and reworking the equations (18) to (21), it will give four ordinary differential equations:

$$\frac{du_{z*}}{dz_*} + 2u_{r*} = 0 \qquad (29)$$

$$\frac{d^2u_{r*}}{dz_*{}^2} - u_{z*}\frac{du_{r*}}{dz_*} - u_{r*}^2 + u_{\varphi*}^2 = 0 \qquad (30)$$

$$\frac{d^2u_{\varphi*}}{dz_*{}^2} - u_{z*}\frac{du_{\varphi*}}{dz_*} - 2u_{r*}u_{\varphi*} = 0 \qquad (31)$$

$$\frac{d^2u_{z*}}{dz_*{}^2} - u_{z*}\frac{du_{z*}}{dz_*} - \frac{dp_*}{dz_*} = 0 \qquad (32)$$

The non-slip boundary conditions for $z > 0$ and $r < b$ at a rotating surface are transformed to:

When $z_* = 0$

$$\left.\begin{aligned} u_{z*} &= 0 \\ u_{\varphi*} &= 1 \\ u_{r*} &= 0 \\ p_* &= 0 \end{aligned}\right| \qquad (33)$$

And when z approaches ∞

$$\left.\begin{aligned} u_{\varphi*} &= 0 \\ u_{r*} &= 0 \end{aligned}\right| \qquad (34)$$

Owen and Rogers (1989) gave a numerical solution of the dimensionless system of equations (29) to (32), for non-slip conditions. A graphical plot of the solution is shown in Figure 11.

This solution enables us to calculate velocities at any point of the induced flow as long as the disk radius and the angular velocity are both known. The kinematic viscosity of the fluid has to be defined as well. In order to calculate any dimensionless variables, formulae (24) to (28) apply.

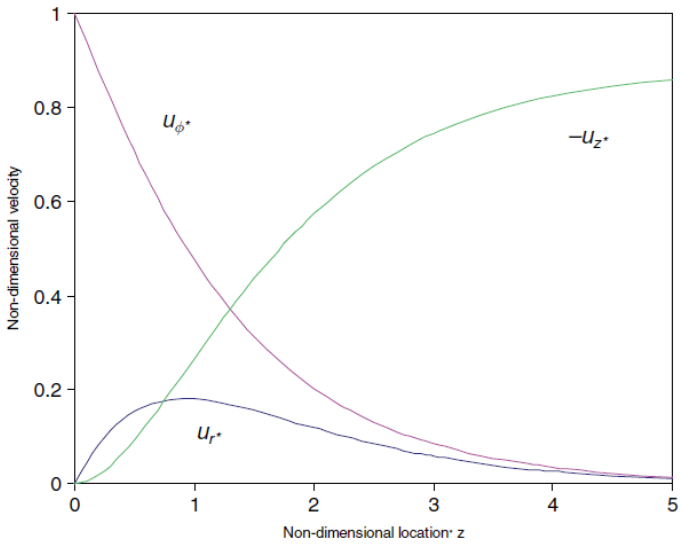

Figure 11. Dimensionless velocity profile for laminar flow at free disk (Peter R.N Childs, 2011)

The required torque to rotate a disc with specific radius and angular velocity may be obtained by integrating the tangential component of the fluid stress at the surface over the area of the disc, i.e.

$$T_q = \tau \Omega r \tag{35}$$

The tangential component of the shear stress is

$$\tau_\varphi = \mu \left[\frac{\partial y}{\partial x}\right]_{z=0} \tag{36}$$

By partial differentiation of equation (26) transposed to $u_\varphi = u_{\varphi *} r\Omega$, in respect of z, it becomes:

$$\frac{\partial u_\varphi}{\partial z} = r\Omega \frac{\partial u_{\varphi *}}{\partial z} \tag{37}$$

The same is done for equation (24) resulting in following equation:

$$\frac{\partial z_*}{\partial z} = \sqrt{\frac{\Omega}{\nu}} \tag{38}$$

Substituting ∂z into equation (37) gives:

$$\frac{\partial u_\varphi}{\partial z} = \frac{r\Omega^{1.5}}{\sqrt{\nu}} \frac{\partial u_{\varphi *}}{\partial z_*} \tag{39}$$

This equation gives the link between dimensional and non-dimensional expression of the tangential component of the stress on the surface of the disk.

In order to show the frictional torque over entire disk surface, we have to consider an elemental ring of the disc. Its area is $\delta A = 2\pi r \delta r$. The frictional moment, i.e., T_q, will be derived by integrating the tangential component of the fluid stress over the disk.

$$T_q = -\int_0^b 2\pi r \times \mu \left[\frac{\partial u_\varphi}{\partial z}\right]_{z=0} \times r dr$$

$$= -\int_0^b 2\pi r^2 \mu \frac{r\Omega^{1.5}}{\sqrt{\nu}} \left[\frac{\partial u_{\varphi *}}{\partial z_*}\right]_{z_*=0} dr \qquad (40)$$

$$= -\int_0^b 2\pi r^3 \mu \frac{r\Omega^{1.5}}{\sqrt{\nu}} \left[\frac{\partial u_{\varphi *}}{\partial z_*}\right]_{z_*=0} dr$$

It results in:

$$T_q = -0.5\pi b^4 \rho \nu^{0.5} \Omega^{1.5} \left[\frac{\partial u_{\varphi *}}{\partial z_*}\right]_{z_*=0} \qquad (41)$$

Calculations associated with the experiment are in subsection 5. 3. 3.

4. 4. Rotating cylinders

A flow between two rotating coaxial cylinders is considered. This is shown in Figure 12. This type of flow is well explored, and the existing knowledge is used in this work to determine the required torque for rotating the inner cylinder.

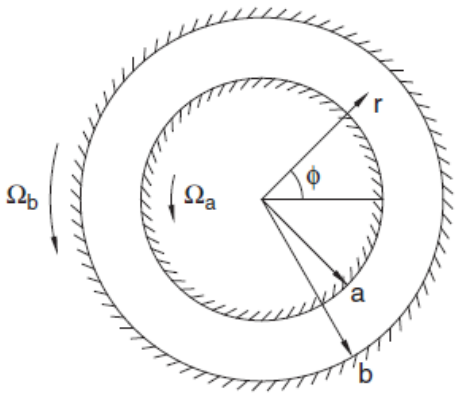

Figure 12. Rotating concentric cylinders flow, Childs (2011)

The rotating speed of the inner cylinder is Ω_a and the rotating speed of the outer cylinder is Ω_b. Four dimensionless control parameters characterise the system. These are radius ratio, $\eta = \frac{a}{b}$; aspect ratio, $\Gamma = \frac{Length\ of\ the\ cylinder}{b-a}$, rotation ratio, $\frac{\Omega_b}{\Omega_a}$ and rotational Reynolds number of the inner cylinder, equation (42). In the current set up the outer cylinder is stationary. Consequently, the rotation ratio is zero.

Peter R. N. Childs (2011) gives following formula for the rotational Reynolds number

$$R_e = \frac{\Omega r_i d}{\nu} \tag{42}$$

where, R_e is the Reynolds Number

Ω is the angular velocity of the inner cylinder

r_i is the radius of the inner cylinder

d is the gap between inner and outer cylinder

ν is the kinematic viscosity of the water.

The Navier-Stokes equations in cylindrical polar coordinates (13), (14), (15) and the continuity equation (17) describe the rotational flow. For boundary non-slip conditions this configuration yields the followings:

$$\begin{aligned} u_r = u_z = 0 \quad at \quad r = a, r = b \\ u_\varphi = \Omega_a a \quad at \quad r = a \\ u_\varphi = \Omega_b b \quad at \quad r = b \text{ and } p = p_b \end{aligned} \tag{43}$$

In the experimental set up the outer cylinder is stationary, so $\Omega_b = 0$

4. 4. 1. Laminar flow.

At laminar flow, axial and radial components of the velocity field are zero. Then the continuity (17), in cylindrical coordinate system, is reduced to:

$$\frac{\partial u_\varphi}{\partial \varphi} = 0 \qquad (44)$$

Hence, the Navier-Stoke equations (4), (5) and (6) are reduced to:

$$-\frac{\rho u_\varphi^2}{r} = -\frac{dp}{dr} \qquad (45)$$

$$0 = \mu\left(\frac{d^2 u_\varphi}{dr^2} + \frac{1}{r}\frac{du_\varphi}{dr} - \frac{u_\varphi}{r^2}\right) \qquad (46)$$

These equations can be solved analytically at boundary conditions without slip, equation (43).

Equation (46) is solved by a standard solution in the form of

$$u_\varphi = C_1 r + \frac{C_2}{r} \qquad (47)$$

where,

$$C_1 = \frac{\Omega_b b^2 - \Omega_a a^2}{b^2 - a^2} \qquad (48)$$

$$C_2 = \frac{(\Omega_a - \Omega_b) b^2 a^2}{b^2 - a^2} \qquad (49)$$

After substitution of equation (47) into equation (45) pressure distribution will be expressed as follows:

$$\frac{dy}{dx} = \rho\left(C_1^2 r + 2\frac{C_1 C_2}{r} + \frac{C_2^2}{r^3}\right) \tag{50}$$

After integration, pressure as a function of the radius r is:

$$p = \rho\left(C_1^2\frac{r^2}{2} + 2C_1 C_2 lnr - \frac{C_2^2}{2r^2}\right) + C \tag{51}$$

Where C is an integration constant and has to be defined for the specific conditions of the problem, i.e., at $r = a$, $p = p_a$ and at $r = b$, $p = p_b$

In order to define the torque required to rotate the inner cylinder at a certain angular velocity, it is necessary to specify the viscous shear stress at the surface of the cylinder. Hence:

$$\tau = \mu\frac{r\partial\left({}^{u_\varphi}/_{r}\right)}{\partial r} \tag{52}$$

Since u_φ as a function of r is already specified in equations (47), (48) and (49), differentiation can be performed, and it results in:

$$\tau = -2\mu\frac{(\Omega_a - \Omega_b)b^2}{b^2 - a^2} \tag{53}$$

In this theoretical view, the cylinders are infinitely long. That is why it is important to specify torque per unit length H. It is $\frac{\tau A a}{H}$, where A is the surface area of the cylinder. It can be defined by:

$$A = 2\pi aH$$

Then the torque is:

$$T_q = \frac{\tau(2\pi aH)a}{H} = 2\pi a^2\tau \qquad (54)$$

Substituting formula (53) for the viscous shear stress into equation (54), the torque required per unit length becomes:

$$T_q = 4\pi\mu\frac{b^2a^2}{b^2 - a^2}(\Omega_b - \Omega_a) \qquad (55)$$

Laminar flow is defined when the Taylor number for mean annulus radius, Equation (56), is below the critical Taylor number. For a narrow gap and a stationary outer cylinder, it is 41.19, (Childs, p. 185). Higher values of the Taylor number mark the transit to the instability of laminar flow and possible formation of vortices in the flow between the cylinders.

The Taylor number is defined by the formula as follows:

$$T_{am} = \frac{\Omega r_m^{0.5}(b-a)^{1.5}}{\nu} \qquad (56)$$

where,

$r_m = \frac{a+b}{2}$

Since the Reynolds number is used in this study to establish the flow regime, the critical rotational Reynolds number is calculated accordingly for the experimental set up. The critical rotational Reynolds number is 75.

4. 4. 2. Turbulent flow.

At larger Reynolds numbers, inertial forces in the flow are larger than viscous forces. This leads to the appearance of turbulence. For rotational flows, the formation of vortices is due to centrifugal forces initially and, with an increase of Reynolds number, shear forces take dominance in the turbulence formation. (Lathrop, 1992)

For turbulent flow, the Navier-Stokes equations (13), (14), (15) and the continuity equation (17) in a cylindrical coordinate system describe the flow motion. The boundary non-slip conditions are:

$u_\varphi = \Omega_a a \quad at \quad r = a$ and

$u_\varphi = \Omega_b b \quad at \quad r = b$

$u_r = 0 \quad \text{and} \; u_z = 0 \quad \text{at} \quad r = a \,\text{and}\, r = b$

But, within the gap $u_r \neq 0\,, u_z \neq 0$ and together with u_φ, they are dependent on r, φ and z. In addition, for the turbulent case, simplifications such as $\partial_\varphi \approx 0$ are not acceptable.

Taylor-Couette flow is a flow in a fluid in the gap between two rotating co-axial cylinders generated by that rotation. Thermal Tayleigh-Benard convection is a flow in a fluid generated by heat coming from the underside of a fluid layer.

Eckhardt, Grossmann and Lohse (Eckhardt, Grossmann, & Lohse, 2007) found there was a strong analogy between Taylor-Couette flow and thermal Tayleigh-Benard convection. Using the basic quantities of these two theories and their relations, Eckhardt,

Grossmann and Lohse defined torque as a function of the angular velocity and radius ratio, $\eta = \frac{a}{b}$ or gap (the difference of the radii of outer and inner cylinders).

$$T_q = 2\pi\rho H J^{\omega} \tag{57}$$

where,

ρ is the density measured in $[kg/m^3]$

H is the length of the cylinder in $[m]$

J^{ω} is a constant representing the conserved transverse current of rotational motion. Its units are are $[m^4/s^2]$. This quantity is similar to the conserved current of temperature, J in thermal Tayleigh-Benard convection and it can be derived from the measured torque.

By definition, however, angular velocity current, J^{ω}, is defined as:

$$J^{\omega} = r^3 \left[\langle u_r \omega \rangle_{A,t} - \nu \frac{\partial \langle \omega \rangle_{A,t}}{\partial r} \right] \tag{58}$$

where the first term, in square brackets, reflects 'Reynolds stress' and the second term reflects viscous derivative and is analogous to heat current,

u_r is the radial velocity

ω is the angular velocity

ν is the kinematic viscosity

r is the local radius.

For the inner cylinder, $r = a$, the velocity current takes the form of:

$$J^{\omega}|_{r=a} = a^3 \nu \frac{\partial \omega}{\partial r}|_{r=a} \tag{59}$$

Dimensionless torque, G, can be defined as:

$$G = \frac{T_q}{2\pi\rho\nu^2 H} = \frac{J^{\omega}}{\nu^2} \tag{60}$$

4. 5. Ship resistance

The total resistance of a ship is defined by many factors. For determining hull resistance in calm water, the upright resistance or total resistance may be divided into components such as wave making, pressure and viscous resistance. Wave making and pressure resistance are dependent on the shape of the hull and are not relevant to this study.

Viscous resistance is a complex component and attributable to the viscosity of the water. While viscous form resistance is highly influenced by the shape of the hull, skin friction depends more on the properties of the surface of the submerged part of the hull and the speed. The latter is relevant to this study.

Skin friction is affected by the regime of the flow: laminar or turbulent. Along the waterline, a transition from one to the other occurs. The further from the bow entrance this transition happens, the more beneficial it is for reducing of the friction. The regime is defined by the Reynolds number:

$$R_n = \frac{VL}{\nu}, \tag{61}$$

where,

R_n is the Reynolds number

ν is the kinematic viscosity of the water

V is the velocity

L is the length of the waterline of the vessel.

The Reynolds number (*Rn*) is a dimensionless number and at a value *Rn* of 4.5×10^5 or above, the transition to turbulent flow may occur (Lewis, 1988). The actual value of the Reynolds number when transition does occur depends on a number of factors such as the shape of the object entering water (bowlines) or roughness of the surface or, possibly, the slip conditions.

In Naval Architecture, all calculations are done at non-slip conditions. It includes calculations of friction resistance, R_F.

$$R_F = C_F 0.5 \rho S V^2 \quad (62)$$

where,

R_F is the friction resistance

ρ is the density of the water

V is the velocity

S is the wetted surface

C_F is the friction coefficient.

The friction coefficient for laminar flow can be defined by using the Blasius line, where:

$$C_F = 1.327(R_n)^{-0.5} \quad (63)$$

where,

C_F is the friction coefficient

R_n is the Reynolds number

The friction coefficient for turbulent flow is derived from a modified Schoenherr line, accepted in 1957 by International Towing Tank Conference, (Lewis, 1988) and is expressed by the equation (64) as follows:

$$C_F = \frac{0.075}{(\log_{10} R_n - 2.0)^2} \quad , \quad (64)$$

where,

C_F is the friction coefficient

R_n is the Reynolds number.

The friction resistance R_F of a ship is evaluated as a part of the procedure for establishing total resistance of the ship. In this procedure, an allowance C_A is introduced. If a total friction coefficient is C_T, then:

$$C_A = C_{T(measured)} - C_{T(estimated)} \, , \quad (65)$$

In resistance evaluation a variety of methods are used for example:

- Traditional and standard series methods
- Regression based methods
- Direct model tests
- Computational Fluid Dynamics

In this thesis, direct model tests are used. The general concept of this method is as follows.

A model of the ship is manufactured at a scale so that the model's submerged cross-section is less than 0.4% of that of the towing tank in order to avoid interference with walls and the bottom of the tank. The finish of its surfaces is required to be to a very high degree of smoothness and turbulence stimuluses are placed at the bow to simulate the transition from laminar to turbulent flow. The model is attached to a carriage in a way that allows for heave and pitch vertically while measuring the horizontal towing force. The hull is ballasted giving the correct position and level of the waterline for the model. Testing is conducted at various speeds (Phillips-Birt, 1970).

In general, the resistance of the ship is scaled from the measured forces using ship-model scale factor, form coefficient and resistance component giving allowance for factors like skin roughness, uninstalled model appendages, air drag, including components present on the ship, but not on the model, (Carlton, 2007). Friction resistance components of the model and the ship are calculated rather than measured and scaled.

Since this method is based on similar wave making and form viscose resistance combined for the ship and model but not on similar friction conditions, this method makes it not applicable when studying frictional resistance alone.

A simple ship resistance decomposition method is used in this study:

$$R_T = R_F + R_R \tag{66}$$

where,

R_T is Total ship resistance

R_F is Frictional resistance

R_R is Residual resistance, as well known as pressure resistance, which is combined wave-making and viscous pressure resistance.

In this work, however, scaling may be used in case differences in the measured towing forces between treated and non-treated vessel occur. For the specific set up of the towing tank experiment, see section 6. 2.

Chapter

5. Experimental Investigation: setup, result and discussion

5. 1. Introduction

This chapter begins with statistical methods used in all experimental work and it is presented in section 5. 2. It is followed by laboratory work execution and outcomes. Section 5. 3 presents an initial assessment of drag reduction, gives general information about the setup of the rotating disk experiment and the calculations associated with the test and results. It is important to remember that the rotational Reynolds number along the radius varies. The observed phenomenon of slip provides a basis for further studies. Section 5. 4 covers the rotating co-axial cylinders experiments and gives detailed information about the experimental setups at specific rotational Reynolds numbers. The section ends with the results of these experiments for both treated and non-treated (neat) surfaces and compares them.

5. 2. Statistical methods used in this study

The assessment of accuracy of measured quantities and the reliability of the results are an important part of any experimental study. This is the area where statistical methods are involved.

5. 2. 1. Sampling

In order to obtain unbiased results, the measurements need to be taken under unchanging conditions thereby eliminating sources of potential errors. That is why each

experiment was repeated at least five times on different days and/or the settings were reassembled in between. Hence, it can be considered as random sampling.

5. 2. 2. Mean, variance and standard deviation

The sample mean value of the measured parameters i.e. torque or force, was calculated by:

$$\bar{x} = \frac{x_1 + x_2 + \cdots + x_n}{n} = \frac{\sum_{i=1}^{n} x_i}{n} \quad (67)$$

where,

$\bar{x}$ is the mean value

$x_1, x_2, \ldots, x_i$ is the value of the parameter at experiment 1, 2, …, i

n is the number of experiments.

The mean value is an unbiased estimator of the parameter, but it does not provide the full picture of the testing conditions and reliability of the data is not estimated. This is the reason for calculating a variance of the sample and the standard deviation. The latter gives a standard error of the measured parameter. The following formula is used for these calculations (Montgomery, 2018):

$$s^2 = \frac{\sum_{i=1}^{n}(x_i - \bar{x})^2}{n - 1} \quad (68)$$

where,

s is the standard deviation of the sample

$x_1, x_2, \ldots, x_i$ is the value of the parameter at experiment 1, 2, …, i

n is the number of experiments.

5. 2. 3. Standard error of the mean.

While the standard deviation reflects varying values of the measurements in the experiments, the standard error of the mean relates it to the population. In other words, it shows an uncertainty of the estimated mean. The standard error of the mean is defined by the following equation (Peters, 2001):

$$s_{\bar{x}} = \frac{s}{\sqrt{n}} \qquad (69)$$

where,

$s_{\bar{x}}$ is the standard error of the mean

s is the standard deviation of the sample

n is the number of experiments.

5. 3. Initial assessment of drag reduction: setup and results.

The purpose of the experiment is to establish if the surface fabricated by the methods described in Section 3.3., has the expected drag reducing ability when in a solid water flow i.e., the water does not contain air bubbles and no external disturbances (waves or flow) are present.

5. 3. 1. Experimental rotating disk tests

The general idea for drag reduction assessment is to measure and compare forces required for a plate, treated and untreated, towed through water or held when washed by a water flow.

The published methods for the purpose of assessment of drag reduction are associated with expensive equipment like a plate set in a water tunnel (Park, Sun, & Kim, 2014;(Ünal et al., 2012)) or a complex piping system (Berg et al., 2008; Brockman, 1957; Watanabe, 1999).

For the initial assessment, it is more practical to use available equipment, accessible materials and established methods. Rotating flow, specifically the rotating disk, is well studied and suitable for this purpose. Instead of comparing forces, the measured torque is compared. The rotating disc is a useful start up since it combines both laminar and turbulent flow effects since close to the axis, the flow is expected to be laminar, while at the edge of the disc it can be turbulent. (Peter R.N Childs, 2011)

5. 3. 2. Instrumentation and model construction.

In order to measure the torque required to rotate a disk submerged in the water at a specific RPM, a suitable device is needed. The chosen device is a Brookfield Dial Reading Viscometer RV model, see Figure 13.

Figure 13. Analogue reader of the rheometer.

The Brookfield viscometer is designed to measure the torque required to rotate calibrated disks or cylinders submerged in a viscous substance. This measurement is easily transformed to a viscosity, applying predetermined coefficients depending on the tool used, (BROOKFIELD, n.d). Consequently, this design allows the device to be used for torque measurements without any further adjustments. However, there are some limitations associated with the use of the machine. The *Brookfield* viscometer measures torque at fixed rotational speeds of 10, 20, 50 and 100 RPM.

In addition, the standard disks are small in diameter. This design is to measure higher viscosities than that of water. The material of these disks differs from the one chosen for the experiment as well. New discs were fabricated for this study and glued to the original spindle.

The fabricated new discs complied with two conditions.

1. The area of the disk has to be sufficient to require a measurable torque when rotating at the specified RPM
2. The moment of inertia of the disk has to be within the inertia range of the original disks used by the apparatus.

A disc with diameter of 140 mm and thickness of 1mm met these requirements. The weight of the disc with this geometry was 49 g.

A stainless-steel cylinder four litres in volume was filled with two litres of deaerated tap water. The amount of water was dictated by practicality, so as not to spill over during the test but also to cover the rotating discs with a layer of 100 mm. This layer creates a small hydrostatic pressure and is larger than the boundary layer that was calculated using methods described in Rotating Flow by Childs, P. R. N. (2011).

It is important to take the reading at a stabilised mode, i.e., in an established steady flow pattern. To ensure a steady flow, the reading is taken after 2 minutes of rotation. The reading has to be constant, although in some cases some pulsation in reading may occur (Brookfield, n.d.).

The device compares the experimental torque to a reference torque. Reference torque for this model is 7187.0 dyne-cm or 0.7187 mNm, (BROOKFIELD, n.d). The experimental data give percentages of the reference torque used to calculate the actual torque. At 10 rpm, the percentage turns out to be too small, below 10% of the maximum reading, which is not recommended by the manufacturer and is not reliable. Readings at 100 rpm were more than 100%, i.e., exceeding the torque range of the device. Consequently, a reasonable comparison of the torque required the speed of rotation of treated and non-treated disks to be limited to 20 and 50 rpm.

Five consequent repetitions of the test were done for each of the rotational speeds using neat, i.e. non-treated and SLIPS, i.e. treated disks.

In order to ensure the readings were correct, calculations were done for the expected torque according to the theory (see the next subsection 5. 3. 3.).

The measured torque, torque reduction and theoretical values of torque were calculated and are shown in the subsection 5. 3. 4.

5. 3. 3. Data analysis for the rotating disk experiment

5. 3. 3. 1. Flow regime

In order to establish the flow regime, rotational Reynolds numbers were calculated. Using formula (16), the greatest local rotational Reynolds number was computed, and the flow regime defined respectively. The values of ρ and μ for fresh water at 22 ºC, as measured during the experiment, are as follows:

$$\rho = 998.5\ kg/m^3$$

$$\mu = 0.000956\ Pa\ s$$

Equation (16) is slightly modified to include a conversion for angular velocity from rotational frequency (RPM) to radians per second, since $\Omega = \mathrm{RPM} \times \frac{2\pi}{60}$,

$$\mathrm{Re}_{\varphi,\ \mathrm{local}} = \frac{\rho(\mathrm{RPM} \times \frac{2\pi}{60})\mathrm{r}^2}{\mu} \qquad (70)$$

For 10 rpm $Re_{\varphi,\ local} = \frac{998.5\ (10\times\frac{2\pi}{60})0.07^2}{0.000956} = 5362\ < 1.78\times10^5$

For 20 rpm $Re_{\varphi,\ local} = \frac{998.5\ (20\times\frac{2\pi}{60})0.07^2}{0.000956} = 10724 < 1.78\times10^5$

For 50 rpm $Re_{\varphi,\ local} = \frac{998.5\ (50\times\frac{2\pi}{60})0.07^2}{0.000956} = 26810 < 1.78\times10^5$

For 100 rpm $Re_{\varphi,\ local} = \frac{998.5\ (100\times\frac{2\pi}{60})0.07^2}{0.000956} = 53622 < 1.78\times10^5$

Transit from laminar to turbulent flow began at about $Re_{\varphi,\ local} = 3.1\times10^5$ for the polished rotating disk and at about 2.2×10^5 for the roughened disk (Theodorcen, 1944). Another study shows a transition beginning at about $Re_{\varphi,\ local} = 1.78\times10^5\ to\ 2.12\times10^5$ (Gregory, 1955).

Consequently, in all four cases, laminar flow is expected.

5. 3. 3. 2. Boundary layer thickness

The disk diameter in this set of experiment is 140 mm. It rotates with angular velocity of 50 RPM. The kinematic viscosity of water at 22 ºC is:

$$\nu = \frac{\mu}{\rho} = \frac{0.000956}{998.5} = 0.96\times10^{-6}\ \frac{m^2}{s}$$

Let us look at an arbitrary point above the rotating disk defined by r = 35 mm and z = 1 mm above it.

The non-dimensional location is defined by equation (24).

$$z_* = z \sqrt{\frac{\Omega}{\nu}} = 0.001 \sqrt{\frac{50 \times 2\pi/60}{0.96 \times 10^{-6}}} = 2.3 \quad (71)$$

Entering the calculated non-dimensional value for z_* into the numerical solution of the Navier-Stokes system of equations, we can derive non-dimensional values for u_{r*}, $u_{\varphi*}$, $u_{\varphi*}$, u_{z*} and p_*.(Owen, 1989) Substituting these values in equations (25) to (28) the actual velocities and pressure are solved i.e.

$$\begin{aligned} u_r &= u_{r*} r\Omega = 0.0976 \times 0.035 \times 50 \times \tfrac{2\pi}{60} = 0.179\ m/s \\ u_\varphi &= u_{\varphi*} r\Omega = 0.1565 \times 0.035 \times 50 \times \tfrac{2\pi}{60} = \ 0.029\ m/s \\ u_z &= u_{z*}\sqrt{\nu\Omega} = (-0.6380)\sqrt{0.96 \times 10^{-6} \times 50 \times \tfrac{2\pi}{60}} = 0.0045\ m/s \\ p &= -p_* \mu\Omega = -0.3987 \times 0.000956 \times 50 \times \tfrac{2\pi}{60} = -0.002\ Pa \end{aligned} \quad (72)$$

The thickness of the boundary layer can also be defined using this solution. It is the axial distance from rotating disc where tangential velocity is 1% of that of the disk. This occurs at non-dimensional distance $z_* = 5.5$.

Applying equation (24), the actual thickness of the boundary layer is

$$\delta = z = \frac{z_*}{\sqrt{\frac{\Omega}{\nu}}} = \frac{5.5}{\sqrt{\frac{50 \times \frac{2\pi}{60}}{0.96 \times 10^{-6}}}} = 0.0023\ m \quad (73)$$

5. 3. 3. 3. Torque calculations

Since in the experimental part of this project the measured component is the torque, it is critical to calculate its value.

Using the numerical solution of Navier-Stokes equations at non-slip conditions:

for $z_* = 0$, $\frac{\partial u_{\varphi *}}{\partial z_*} = -0.6159.$

By substituting this value into equation (41), we can calculate the torque for one side of the disc, i.e.

$$T_q = -0.5\pi b^4 \rho \nu^{0.5} \Omega^{1.5} \text{(-0.6159)} = 0.9674 b^4 \rho \nu^{0.5} \Omega^{1.5} \quad (74)$$

5. 3. 4. Rotating disk experiment results.

The results from the rotating disk experiments are shown in Tables 2 and 3. As mentioned in subsection 5. 3. 2., the device allows only four fixed angular velocities 10, 20, 50 and 100 RPM. At 100 RPM, however, the expected torque exceeds the capacity of the viscometer and consequently only three rotational speeds were used.

Five repetitions of the test were carried out at each of the rotational speeds. The mean value, sample variance and standard deviation were calculated according to formulae in section 5. 2. and shown in Tables 2 and 3.

The theoretical values of the torque for both sides of the disc were calculated using Equation (74).

Table 2 shows the mean value of the measured torque for the non-treated rotating disks and Table 3 shows the mean value of the measured torque for the treated rotating disks.

Table 2. Measured and calculated torque for non-treated disc at different RPMs.

Torque required for different RPMs	Calculated Torque [mNm]	Measured Mean Torque [mNm]	Variance [mNm]	Standard Deviation [mNm]
10 RPM	0.0486	**0.0419**	1.18E-06	0.0011
20 RPM	0.1375	**0.1161**	2.99E-06	0.0017
50 RPM	0.5437	**0.5373**	0.00015201	0.0123

For the non-treated disk experiment, it can be seen that at low rpm there is about 13-14% difference between the calculated and measured mean value of torque while at 50 RPM, the difference is only 1%.

This can be attributed to the theoretical calculations since they do not consider the gap between the disk and the wall and at low rotational speeds that will have a greater effect on the torque. Another reason is the decrease of the accuracy at the very low measured value of 6.7% of the capacity of the device. But this is not the focus of this study.

Indeed, at 10 RPM the measured torque is 0.0486 mNm, which is definitely less than 10% of 0.7187 mNm or 0.07mNm. The manufacturers explicitly state that measurements below that value are not reliable. Consequently, it was decided to continue with angular velocities of 20 and 50 RPM for the treated rotating disk experiment.

The reliability of the non-treated disk experiment was evaluated by examining the standard deviation. The resulting outcome shows a steady performance giving a narrow band of standard deviation. This allows reliable comparison of the data derived in the tests for the treated and non- treated discs.

Table 3. Torque measured on rotating treated aluminium disc at different RPMs.

orque required for different RPMs	Measured Mean Torque [mNm]	Variance [mNm]	Standard Deviation [mNm]	Percentage change [%]
20 RPM	**0.1125**	1.18E-06	0.0011	3.21
50 RPM	**0.5120**	4.328E-05	0.0066	4.71

In Table 3, showing the data from the treated disk experiment, the mean value of the measured torque, the variance of the readings and the standard deviation are given for 20 and 50 RPM. This table shows additional information, attempting to compare the resistance to rotation of the disks with both types of the surfaces. The mean value of the torque measured at a specific rotational speed for each treated disc is compared to the corresponding value of the measured torque for the non-treated disc using the following equation (75):

$$Percentage\ change\ in\ torque = \frac{T_{q\ non-treated} - T_{q\ treated}}{T_{q\ non-treated}} \times 100, \quad \% \qquad (75)$$

The percentage change in torque required to rotate a disk at a specific angular velocity is positive. It shows that there is a reduction in the drag of 3.21% at 20 RPM and 4.71% at 50 RPM.

A 3-4% drag reduction does not seem to be much but if the total resistance of a ship were to be reduced by that amount, then the power required to propel the vessel through the water would also reduce.

The standard deviation of 0.001 mNm for mean value of 0.112 mNm and 0.006 mNm for 0.52 mNm mean value gives between 0.9 % and 1.2% uncertainty of measurements and it indicates good consistency of the experimental data (see Table 3).

Bearing in mind that the rotational Reynolds number is not constant along the radius of the disk, it does not answer the research question. However, it is a good indication of areas for further study. On the other hand, the chosen measurement tool limited the experiment to two rotational speeds only and that motivates a more detailed study using different techniques.

5. 4. The rotating cylinder experiment: setup and results

5. 4. 1. Experimental setup.

The rotating disk experiment, see section 5. 3., produces a good overall assessment of the effect of SLIPS made in this study with varying local conditions since the Reynolds number changes along the radius. The rotating cylinder experiments focus on one specific condition for the entire surface of the cylinder, so the Reynolds number is constant along the surface. This provides a well-controlled experimental and theoretical environment (Recktenwald, Lücke, & Müller, 1993) to measure the torque required to rotate the inner cylinder of a given diameter. Similar to the disc experiment, the more torque required, the less slippery the cylinder surface is for a given angular velocity. Therefore, it is convenient to use this method; see arrangement in Figure 14.

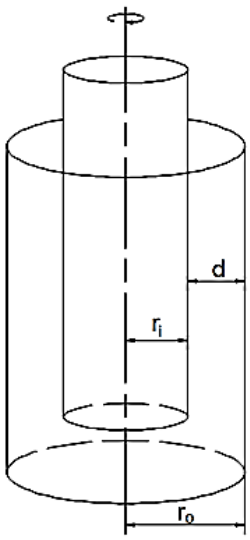

Figure 14. Concentric rotational cylinders setup, where the outer cylinder is stationary.

5. 4. 2. Instrumentation and model construction

A Brookfield Metek rheometer type RST-SST with a digital reader was chosen to measure the torque. This device is primarily designed to measure viscosity which is calculated based on direct measurement of the torque at specific rotational frequencies measured in rotations per minute (RPM) and coefficients associated with the attached tool (vane, cylinder, or disk). The device has been adapted according to the needs of this study, taking readings for the torque and RPM only, see Figure 15.

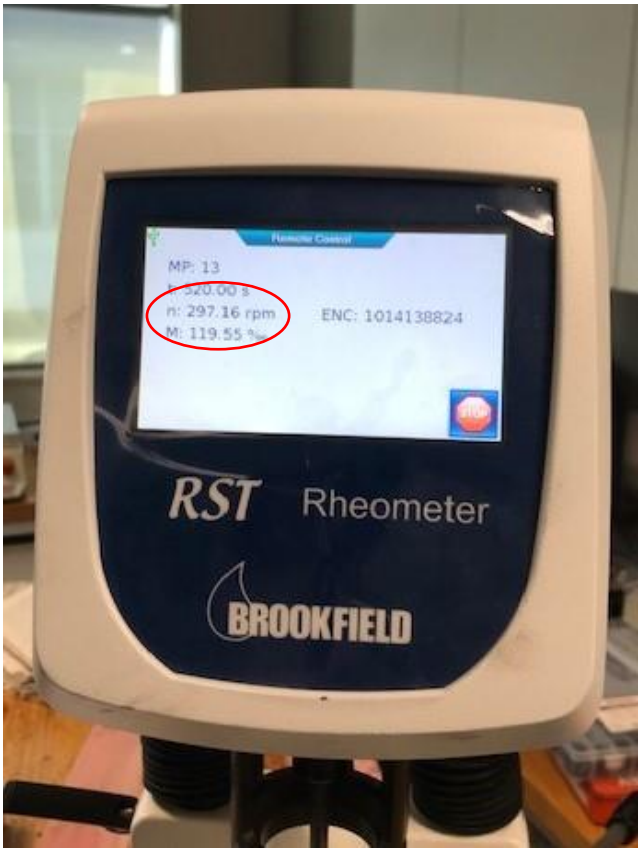

Figure 15. Digital reading

While the rheometer in previous tests uses pre-set speeds, the new rheometer allows for gradual changes in the angular velocity giving precise a reading of the corresponding torque.

The cylinder dimensions were carefully chosen to suit the capacity of the machine. The diameters of the inner and outer cylinders were 100 mm and 140 mm respectively, with a gap of 20 mm. This setting provided sufficient contact area between the inner cylinder surface and the water in order to produce readings of the torque within the full range of the apparatus' capacity.

The rotational speed of the device is limited to 3200 RPM and the maximum torque i.e., capacity is 100 mNm and a resolution is 0.15 µNm.

In order to use the full range of the torque capacity a set of cylinders with different lengths were produced: The longest was 900 mm and was used for low RPMs. The shortest cylinder was 140 mm and used for higher rotational speeds.

Adapters were engineered to attach the cylinders to the existing standard tool. These were produced at AUT's 3D printing lab using technical Nylon, achieving $\pm 0{,}2\ mm$ dimensional accuracy. The role of the attachment system is not only to bring the entire cylinder in contact with the device without any sliding but also to centre and align the inner and outer cylinders. Figure 16 shows the elements of the system. Figure 17 shows the assembly, and Figure 18 shows the complete setup of the rheometer with the installed cylinders ready to go.

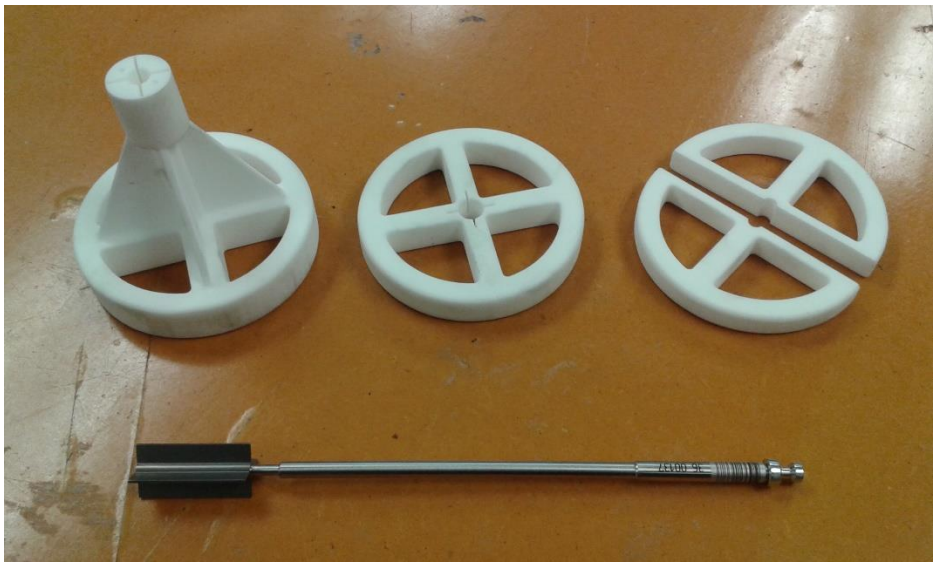

Figure 16. The newly designed and 3D printed parts of the aligning system and a standard vane.

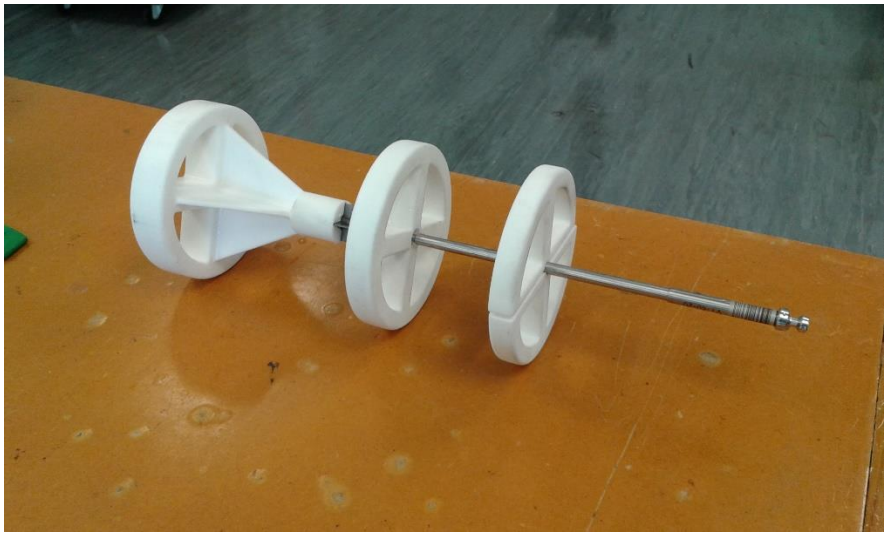

Figure 17. Aligning system attached to a standard vane.

Figure 18. Complete setting with both cylinders installed.

The measured torque is in units of one per thousandths of the capacity, i.e., 1000 ‰ is 100 mNm (Brookfield manual).

A series of tests was conducted for each length of the cylinders, with five repetitions for each condition – SLIPS and neat. Temperature readings were taken manually. The water used was de-aerated at room temperature.

Before each run, the machine needs “zeroing”. This is a process where the friction in the bearings is measured, and the data collected used to adjust measurements during the actual tests.

The machine’s setting allows a gradual increase the angular velocity and it captures the measured torque digitally. The raw data was downloaded to MS Excel files from which calculations for actual torque and the rotational Reynolds numbers were made.

Using this information for treated and non-treated surfaces, the change in the measured torque was assessed using the following equation (76).

$$TR = \frac{TN-TT}{TN} \times 100, \%$$ *(76)*

where,

TR is the torque percentage change,

TN is the torque for the non-treated cylinder in Nm,

TT is the torque for the treated cylinder in Nm.

In order to determine when the change in the flow regime appears, it is important to define the critical Reynolds number.

The critical rotational Reynolds number depends on a number of factors including the cylinders' speed ratio and annulus dimensions. Peter R.N. Childs summarised experimental works of Moalem and Chohen, 1991, and Di Prima and Swinney,1981, in a table showing critical Taylors number (for definition of Taylor number see Equation (56)), for various speed ratios and cylinders radii ratios.

The experimental set up has radii ratio r_{inner}/r_{outer} = 0.7 and speed ratio zero, since the outer cylinder is stationary. The critical Taylor number derived from the Childs' table (p.198) is 52.04. Since the Reynolds number is used in this work, it was calculated using the relation between the two numbers, equation (77). It results from the definitions in equations (42) and (56), when expressing same quantity of Ω/ν. For this experimental set up it is 75.

$$R_e = \frac{T_{am} a(b-a)}{\left(\frac{a+b}{2}\right)^{0.5} (b-a)^{1.5}} \tag{77}$$

5. 4. 3. Rotating co-axial cylinder experiment results and discussions.

The rotating cylinder experiment comprises a range of rotational Reynolds Numbers. The value of each Reynolds number, equation (42), is calculated based on RPM from the raw data digitally captured by the rheometer. As noted above, the recorded torque is in the form of parts per thousand of the capacity. Respectively, it was calculated using the following equation (78):

$$Tq = \frac{M\%}{1000} * Capacity, \ \ mNm \tag{78}$$

where,

$M\%$ is measured torque in parts per thousands

$Capacity$ = 100 mNm, (Rheometer manual).

The aim was to include a large range of Reynolds numbers. Due to limitations of the power of the Rheometer used, three different aspect ratios of the rotating cylinders with different lengths were used. Although the rest of the parameters were kept the same, the rotating cylinders had different wetted areas, so the required torque was measurable for varying rotational speeds and different areas.

The aspect ratios used were 45, 25 and 7, where the aspect ratio is expressed as in equation (79):

$$\Gamma = \frac{Length\ of\ cylinder}{gap\ between\ cylinders} \tag{79}$$

The Reynolds number does not depend on the wetted area of the cylinders, but the torque does. It means that the same torque can be measured for different Reynolds numbers depending on the length of the cylinder. In order to avoid this confusion and to be able to summarise results from all three sets of the tests in one plot, the torque per unit length of the cylinder is considered.

This approach requires eliminating the contribution of the flat bottom part of the cylinders to the torque measured, as the cylinders were closed at the bottom, forming a bottom disk. The torque required for rotating this one-sided disk was calculated using equation (74) and subtracted from the measured torque. After this procedure, the torque per unit length was easily calculated by dividing the result by the length of the tested cylinder.

5. 4. 3. 1. Results from the tests of coaxial cylinders with aspect ratio $\Gamma = 45$

Cylinders geometry:

Inner cylinder diameter is 100 mm

Outer cylinder diameter is 140 mm

Submerged length of the cylinder is 900 mm

Wetted area of the cylinder is 28274 mm^2.

Outer cylinder is stationary

Figure 19. Complete setting for Γ=45

This set-up, see Figure19, allows obtaining rheometer readings of the torque for a rotating Reynolds number from about 50 to 3200. The corresponding RPM are about 0.5 to 30.

The measured mean torque, the calculated torque per unit length and the corresponding statistics are shown in tabular form in Table 4 for the non-treated and in Table 5 for the treated cylinders. Figure 20 illustrates the results graphically.

Table 4. Mean values and corresponding statistics for the mean from coaxial cylinders experiments, described in section 5.4., for non-treated cylinder $\boldsymbol{\Gamma = 45}$

	Mean RPM	**Re**	**Mean torque (mNm)**	**Variance**	**Sample standard deviation (mNm)**	**Standard error of the mean**	**Torque per unit length (mNm/m)**
1	0.5	53	0.2405	0.001332	0.0365	0.0610	0.2671
2	2.614	279	0.3627	0.000473	0.0217	0.0097	0.4020
3	4.72	504	0.4004	9.72E-05	0.0098	0.0044	0.4426
4	6.81	728	0.4524	0.000182	0.0134	0.0060	0.4987
5	8.922	953	0.533	4.22E-05	0.0065	0.0029	0.5862
6	11.06	1182	0.572	4.23E-05	0.0065	0.0029	0.6272
7	13.146	1405	0.6448	0.000114	0.0106	0.0047	0.7057
8	15.264	1631	0.7189	3.38E-05	0.0058	0.0026	0.7853
9	17.356	1855	0.78	0.000718	0.0268	0.0119	0.8504
10	19.47	2081	0.8593	0.000368	0.0191	0.0085	0.9354
11	21.576	2306	0.9542	2.96E-05	0.0054	0.0024	1.0377
12	23.684	2532	1.0543	2.96E-05	0.0054	0.0024	1.1455
13	25.802	2758	1.1843	0.000114	0.0107	0.0048	1.2864
14	27.896	2982	1.3572	0.000156	0.0125	0.0056	1.4749
15	30.004	3207	1.6081	0.001301	0.0360	0.0161	1.7498

Table 5. Mean values and corresponding statistics for the mean from coaxial cylinders experiments, described in section 5.4., for treated cylinder $\boldsymbol{\Gamma = 45}$

	Mean RPM	**Re**	**Mean torque (mNm)**	**Variance**	**Sample standard deviation (mNm)**	**Standard error of the mean**	**Torque per unit length (mNm/m)**
1	0.498	53	0	0	0	0	0
2	2.602	278	0.034	0.00578	0.0760	0.034	0.0368
3	4.712	503	0.096	0.00773	0.0879	0.0393	0.1044
4	6.822	729	0.25	0.00045	0.0212	0.0095	0.2738
5	8.932	954	0.32	0.00035	0.0187	0.0084	0.3495
6	11.04	1180	0.396	0.00048	0.0219	0.0098	0.4317
7	13.144	1405	0.496	0.00013	0.0114	0.0051	0.5404
8	15.25	1630	0.59	0.00015	0.0122	0.0055	0.6422
9	17.356	1855	0.686	0.00013	0.0114	0.0051	0.7459
10	19.464	2081	0.792	0.00017	0.0130	0.0058	0.8607
11	21.572	2306	0.898	0.00022	0.0148	0.0066	0.9753
12	23.682	2532	1.01	0.00025	0.0158	0.0071	1.0963
13	25.786	2757	1.142	0.00027	0.0164	0.0073	1.2395
14	27.898	2982	1.272	0.00027	0.0164	0.0073	1.3802
15	30.002	3207	1.434	8E-05	0.0089	0.004	1.5564

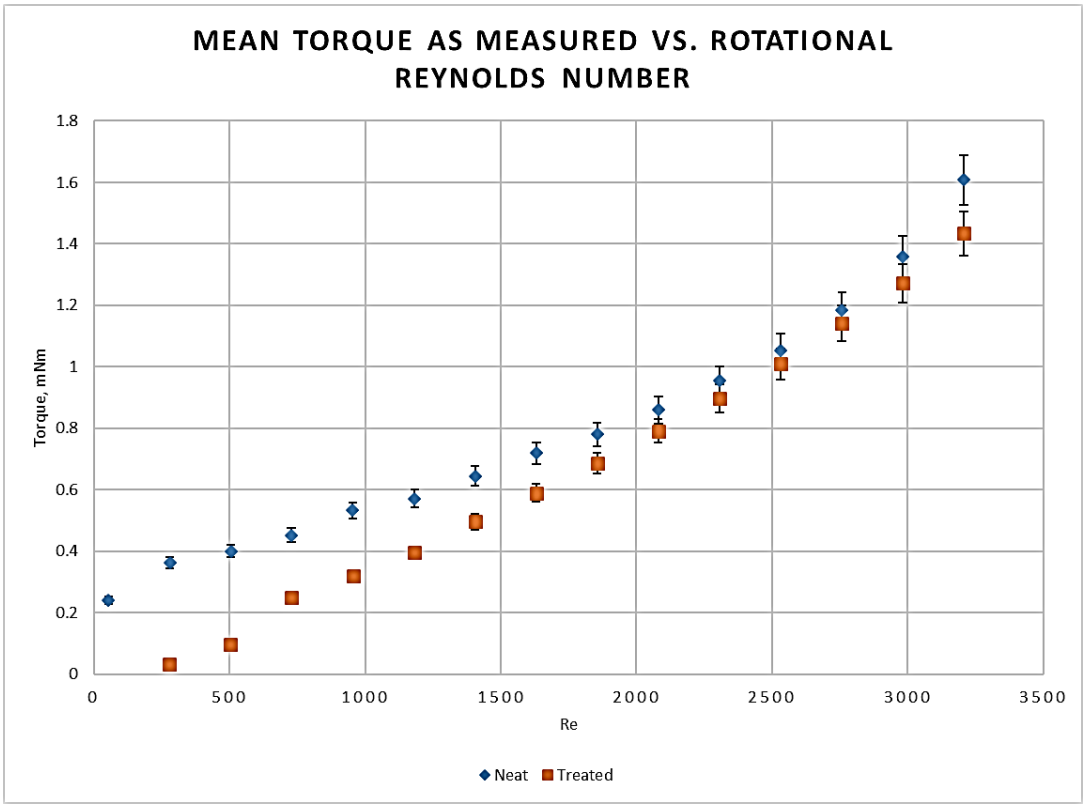

Figure 20. Measured torque for rotating non-treated and treated rotating cylinder with aspect ratio Γ=45 at Reynolds numbers from 53 to 3200

The calculated standard deviation helps to assess the reliability of the collected data. For the non-treated cylinder (Table 4), it can be seen that the standard deviation for a rotational Reynolds number of 53, is 0.0366 mNm at measured torque of 0.2405 mNm. That is15 percent of the value, which is somewhat high. For the treated cylinders (Table 5), at the same rotational Reynolds number of 53, the measured torque is zero. Following the same table up to a Reynolds number of 503, the standard deviation is too high in respect of the measured torque values and is therefore unreliable. Indeed, at an accuracy of the measured torque of 0.1% of the capacity (100 mNm) it is $\pm$0.1 mNm and all values in the range from 53 to 503 are less than that. For example, at Re = 278 the measured torque is 0.034 mNm, it is less than 0.1 mNm and the standard deviation is high 0.0760 mNm.

For the rotational Reynolds numbers from 729 to 3207, although the standard deviation values increase, their percentage of the measured value significantly decrease, from 6% to 0.6%. This type of data, i.e., increase of the accuracy with the increase of the measured value, is typical for scale measuring devices like the rheometer.

Figure 20 shows data for the treated and the non-treated cylinders on the same plot. It allows visualising the differences in the measured torques for both surfaces. The highest decrease of torque in favour of treated cylinders is 44% and appears at the rotational Reynolds number of 729. The smallest decrease is 3.5% at the rotational Reynolds number of 2756. The percentage is calculated using Equation (72).

The observed tendency of diminishing of the required torque with the increase of the Reynolds number can be explained by the increase of the shear hydrodynamic forces in the flow with the further development of the turbulent regime. Thus, these forces become prevalent in the resistance components, which reduces the effect of the skin friction gain within the overall required torque for rotation at a given angular velocity.

5. 4. 3. 2. Results from the tests of coaxial cylinders with aspect ratio $\Gamma = 25$

The geometry of the cylinders is similar to the previous one, but the submerged length is smaller: Inner cylinder diameter is 100 mm

Outer cylinder diameter is 140 mm

Submerged length of the cylinder is 500 mm

Wetted area of the cylinder is 15708 mm^2.

Outer cylinder is stationary

This setting allows obtaining rheometer readings of the torque for the rotating Reynolds numbers from about 1000 to 9500. The corresponding RPM are about 10 to 90.

The measured mean torque, the calculated torque per unit length and the corresponding statistics are shown in Table 6 for the non-treated and in Table 7 for the treated cylinders. To compare the results from the tests a graphical representation is shown in Figure 21.

Table 6. Mean values and corresponding statistics for the mean from coaxial cylinders experiments, described in section 5.4., for non-treated cylinder $\boldsymbol{\Gamma = 25}$

	Mean RPM	**Re**	**Mean torque (mNm)**	**Variance**	**Sample standard deviation (mNm)**	**Standard error of the mean**	**Torque per unit length (mNm/m)**
1	9.998	1068	0.414	0.00308	0.0554	0.0248	0.8152
2	15.71	1680	0.56	0.0014	0.0374	0.0167	1.0948
3	21.426	2290	0.746	0.00178	0.0422	0.0189	1.4519
4	27.128	2900	0.98	0.00065	0.0255	0.0114	1.9028
5	32.85	3512	1.238	0.00022	0.0149	0.0066	2.3998
6	38.534	4120	1.564	0.00023	0.0152	0.0068	3.0312
7	44.278	4734	2.058	0.00667	0.0817	0.0365	3.9967
8	50.004	5346	2.348	0.00182	0.0427	0.0191	4.5529
9	55.716	5957	2.726	0.00013	0.0114	0.0051	5.2837
10	61.42	6566	3.294	0.00043	0.0207	0.0093	6.3932
11	67.13	7177	3.986	0.00178	0.0422	0.0189	7.7494
12	72.866	7790	4.884	0.00588	0.0767	0.0343	9.5162
13	78.572	8400	5.852	0.01627	0.1275	0.0570	11.422
14	84.266	9008	7.608	0.10537	0.3246	0.1452	14.9029
15	90.01	9623	11.444	0.43533	0.6598	0.2951	22.5423

Table 7. Mean values and corresponding statistics for the mean coaxial cylinders experiments, described in section 5.4., for treated cylinder $\boldsymbol{\Gamma = 25}$

	Mean RPM	**Re**	**Mean torque (mNm)**	**Variance**	**Sample standard deviation (mNm)**	**Standard error of the mean**	**Torque per unit length (mNm/m)**
1	10.016	1070	0.2055	0.019714	0.1404	0.0628	0.3983
2	15.714	1680	0.5278	0.011526	0.1073	0.0480	1.0303
3	21.44	2292	0.7344	0.000416	0.0204	0.0091	1.4287
4	27.15	2902	0.9689	0.00241	0.0491	0.0219	1.8805
5	32.854	3512	1.1967	0.003031	0.0550	0.0246	2.3171
6	38.572	4123	1.4478	0.007792	0.0883	0.0395	2.7986
7	44.286	4735	1.7111	0.01391	0.1179	0.0527	3.3029
8	50	5345	2.0033	0.017206	0.1312	0.0587	3.8635
9	55.72	5957	2.2956	0.032855	0.1813	0.0810	4.4228
10	61.43	6567	2.6689	0.037424	0.1934	0.0865	5.1429
11	67.14	7178	3.0578	0.082648	0.2875	0.1286	5.8929
12	72.862	7790	3.5078	0.158478	0.3981	0.1780	6.7638
13	78.574	8400	4.0189	0.299346	0.5471	0.2447	7.7558
14	84.294	9012	4.36	0.145325	0.3812	0.1705	8.4067
15	89.998	9622	4.7922	0.086251	0.2937	0.1313	9.2388

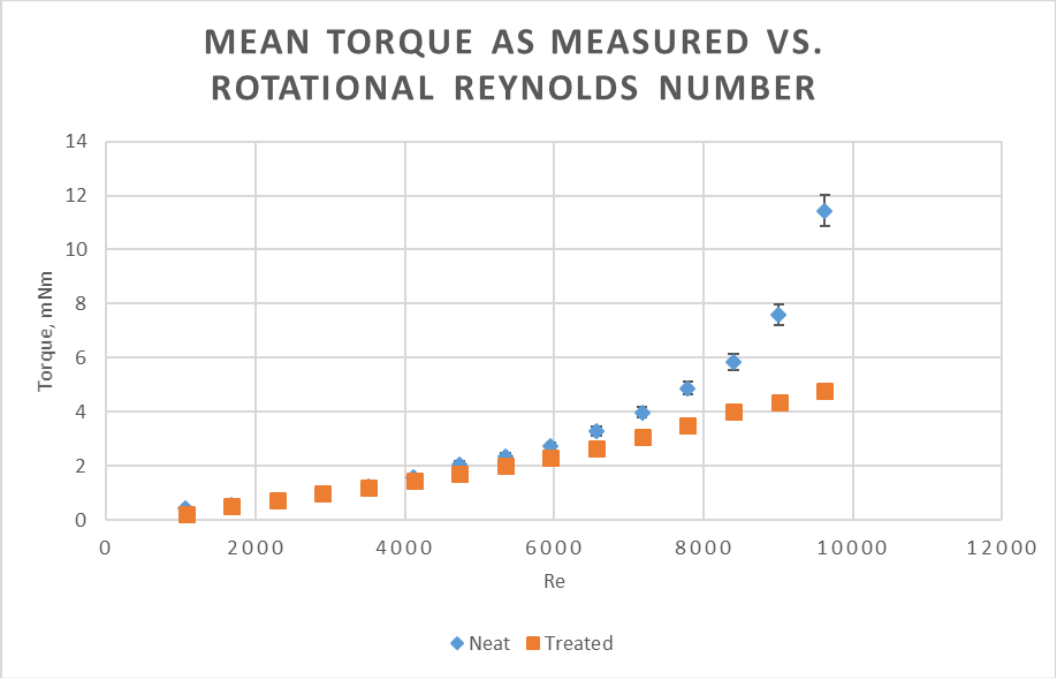

Figure 21. Measured torque for rotating non-treated and treated cylinder with aspect ratio Γ=25 at rotational Reynolds numbers from 1000 to 9600

The change in the mean torque required to rotate the cylinder was calculated for each of the chosen Reynolds numbers. According to these calculations, using equation (72), the smallest decrease in the torque of the treated surface is 1.13 % at Re = 2292 and the highest is 50 % at Re = 9600. A closer look at the data, however, gives a more detailed picture.

Let us consider the difference in the mean measured torque for Re = 1680 for the non-treated and the treated cylinders. It is 0.0322 mNm which is less than the standard deviation for the same measurements for the treated cylinders, which is 0.1073 mNm, i.e. the difference is 0.0322 ± 0.1 mNm. It means that the expected range of values for the difference in the torque is from – 0.0698 mNm to 0.1322 mNm. So, it is better to conclude that the real percentage change in the torque approaches zero. This pattern holds up to Rotational Reynolds number 3500.

Looking at the higher Reynolds numbers within the same setting, the reduction in the torque is significant with the increase in RPM and therefore the Reynolds number. Theoretically, the change in the surface friction for the same surface area should have lesser and lesser effect with increase of the turbulence, which is directly linked to the increase of Reynolds number. The suggested explanation of these results, which are opposite to the theoretical expectations, is as follows:

In this setting of rotating cylinder, the cylinder is suspended on a thin round bar at the one end of a long cylinder. The weight of the cylinder is theoretically considered evenly distributed. Unfortunately, there is always some unbalance in this distribution. Under rotation, this leads to a vibration, an additional source of turbulence, hence the increase of the resistance, which explains quick rise of the torque for the non-treated cylinders.

Furthermore, the vibration of the suspended cylinder will be affected by the correct positioning of the vertical axis around which the cylinder rotates. If that axis is not exactly vertical, the increase of vibration can be expected due to the forces of gravity acting on masses out of the alignment with the axis of rotation. The position of the suspending shaft was controlled as well as the device allows it but still some inconsistency will occur. This can be considered as an experimental error.

Another consideration is that, although the amount of released silicon oil is very small, this may affect the surface tension of the limited amount of liquid within the gap between the cylinders which in turn can change the wave characteristics and their interaction with the surface of the rotating cylinder. Images of the surface waves in the annulus observed during the experiments are captured in Figure 22. The details of this phenomenon are not part of this study.

Figure 22. Surface waves at varying Reynolds numbers

The tendency of an increase in the resistance at higher Reynolds numbers for the non-treated cylinders is obvious for all three aspect ratios. A drop in resistance for treated one is present as well. In the experiment for Γ=25, however, it is somewhat extreme. See Figures 20, 21 and 23.

5. 4. 3. 3. Results from the tests of coaxial cylinders with aspect ratio $\Gamma = 7$

Cylinders geometry:

Inner/outer cylinder diameter is 100 / 140 mm

Submerged length of the cylinder is 140 mm

Contact area of the cylinder is 4398 mm^2.

Outer cylinder is stationary.

This setting allows obtaining rheometer readings of the torque for the rotating Reynolds numbers from about 4000 to 36000. The corresponding RPM are about 40 to 340.

The measured mean torque, the calculated torque per unit length and the corresponding statistics are shown in Table 8 for the non-treated and in Table 9 for the treated cylinders. To compare the mean torque measured for the rotating treated and non-treated cylinders, the results are illustrated in Figure 23.

Table 8. Mean values and corresponding statistics for the mean torque from coaxial cylinders experiments, described in section 5.4., for non-treated cylinder $\boldsymbol{\Gamma = 7}$

	Mean RPM	**Re**	**Mean torque (mNm)**	**Variance**	**Sample standard deviation (mNm)**	**Standard error of the mean**	**Torque per unit length (mNm/m)**
1	40.002	4276	0.394	0.00053	0.0230	0.0103	2.4485
2	61.438	6568	0.8	0.0006	0.0245	0.0109	5.0181
3	82.842	8856	1.318	0.00042	0.0205	0.0092	8.3242
4	104.276	11148	1.936	0.00113	0.0336	0.0150	12.2892
5	125.716	13440	2.63	0.00155	0.0394	0.0176	16.7480
6	147.144	15731	3.482	0.00032	0.0179	0.008	22.2911
7	168.564	18021	4.822	0.00027	0.0164	0.0073	31.2790
8	190.006	20313	5.31	0.0018	0.0424	0.0189	34.1423
9	211.424	22603	6.248	0.00017	0.0130	0.0058	40.1843
10	232.87	24896	7.388	0.00017	0.0130	0.0058	47.6341
11	254.28	27185	8.674	0.00088	0.0297	0.0133	56.0953
12	275.718	29477	10.168	0.00072	0.0268	0.012	66.0100
13	297.154	31769	11.948	0.00027	0.0164	0.0073	77.9376
14	318.57	34058	14.304	0.00023	0.0152	0.0068	93.9514
15	339.996	36349	19.388	0.00557	0.0746	0.0334	129.4226

Table 9. Mean values and corresponding statistics for the mean torque from coaxial cylinders experiments, described in section 5.4., for treated cylinder $\boldsymbol{\Gamma = 7}$

	Mean RPM	**Re**	**Mean torque (mNm)**	**Variance**	**Sample standard deviation (mNm)**	**Standard error of the mean**	**Torque per unit length (mNm/m)**
1	40.002	4276	0.392	0.00437	0.0661	0.0296	2.4342
2	61.432	6567	0.814	0.00613	0.0783	0.0350	5.1182
3	82.858	8858	1.356	0.00173	0.0416	0.0186	8.5954
4	104.264	11147	1.92	0.0041	0.0640	0.0286	12.1752
5	125.722	13441	2.542	0.00312	0.0559	0.0250	16.1192
6	147.146	15731	3.358	0.00142	0.0377	0.0169	21.4053
7	168.554	18020	4.54	0.00075	0.0274	0.0122	29.2650
8	189.99	20312	5.14	0.00325	0.0570	0.0255	32.9284
9	211.43	22604	6.032	0.00047	0.0217	0.0097	38.6413
10	232.862	24895	7.124	0.00118	0.0344	0.0154	45.7487
11	254.282	27185	8.29	0.00085	0.0292	0.0130	53.3524
12	275.728	29478	9.568	0.00117	0.0342	0.0152	61.7239
13	297.148	31768	11.018	0.00082	0.0286	0.0128	71.2950
14	318.566	34058	12.72	0.00015	0.012	0.0055	82.6373
15	340.004	36350	15.264	0.00088	0.0297	0.0133	99.9651

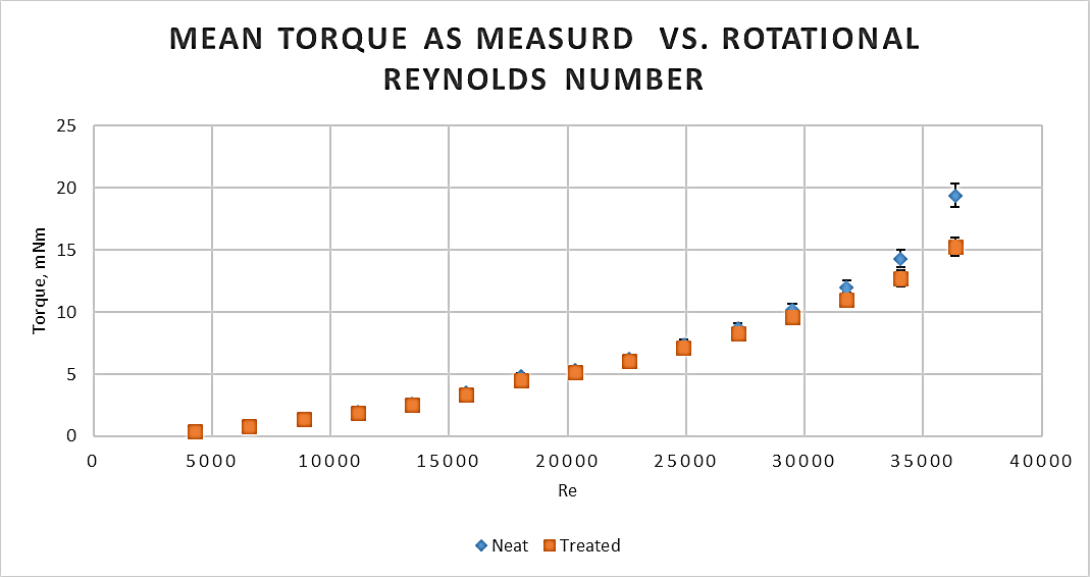

Figure 23. Measured torque for rotating non-treated and treated rotating cylinder with aspect ratio Γ=7 at Reynolds numbers from 4000 to 36000

The change in the required torque for the rotation of treated and non-treated cylinders was calculated according to Equation (76). The smallest difference in the mean value of the measured torque is -2.9% at Reynolds number of 8800. The largest is 21% at Reynolds number 36350. The latter coincided with visual vibration.

Similarly to the results from the tests of coaxial cylinders with aspect ratio Γ=25, for the small measured torques the difference between the torque for the non-treated and the treated cylinders at the same Reynolds numbers is smaller than the standard deviation. For example, at the Reynolds number 6567 the difference in the mean measured torque is -0.014 mNm and the standard deviation for the treated cylinders is 0.0783 mNm. It means that the expected range of the values for the difference in the torque is from –0.0923 mNm to 0.0643 mNm. In that case, the percentage change in the torque again approaches zero. This pattern appears from the Rotational Reynolds number 4276 to 11150.

The reason for these effects is the too-small values of the measured torque in all three cases. For the measuring devices, like this rheometer, typically the accuracy is high for measurements close to the full scale but is less when the measured value is smaller than 10% of the capacity as is the case here.

It is interesting to note that the difference in the required torque to rotate Γ=7 cylinder is maintained the same at Reynolds numbers 13500 to 25000. It is 3.5 % ± 0.2 %. With the visual appearance of a vibration the difference increases up to 20 % at Re = 36350.

The same considerations are applied to this set of experiments as for Γ=25 cylinders. Is the experimental error due to differences in the alignments resulting in the differences in vibrations to be blamed or is it due to change in the wave interaction with the rotating surface of the cylinder? The latter requires further investigation, but it is not relevant to the research question of this work.

Considering all three sets of experiments with different aspect ratios of the cylinders at same radius of inner and outer cylinders, it can be seen that there are very different measured torques for the same Reynolds number. The reason is that the design of the length of the cylinders is linked to the available power of the measuring device. The power requirement is a function of the torque and angular velocity. If a wider range of angular velocities is investigated with respect to Reynolds numbers, the torque has to be manipulated. The latter is a function of the wetted area, which is proportional to the length of the cylinders, when the rest of geometry is the same. Under those circumstances, at the same Reynolds number, different values will be measured for the torque for different lengths of cylinder. In order to summarise the results for a wider range of Reynolds number, the torque per unit length is used, as that will normalise for all three specific lengths of the cylinders. It is shown in Figure 24.

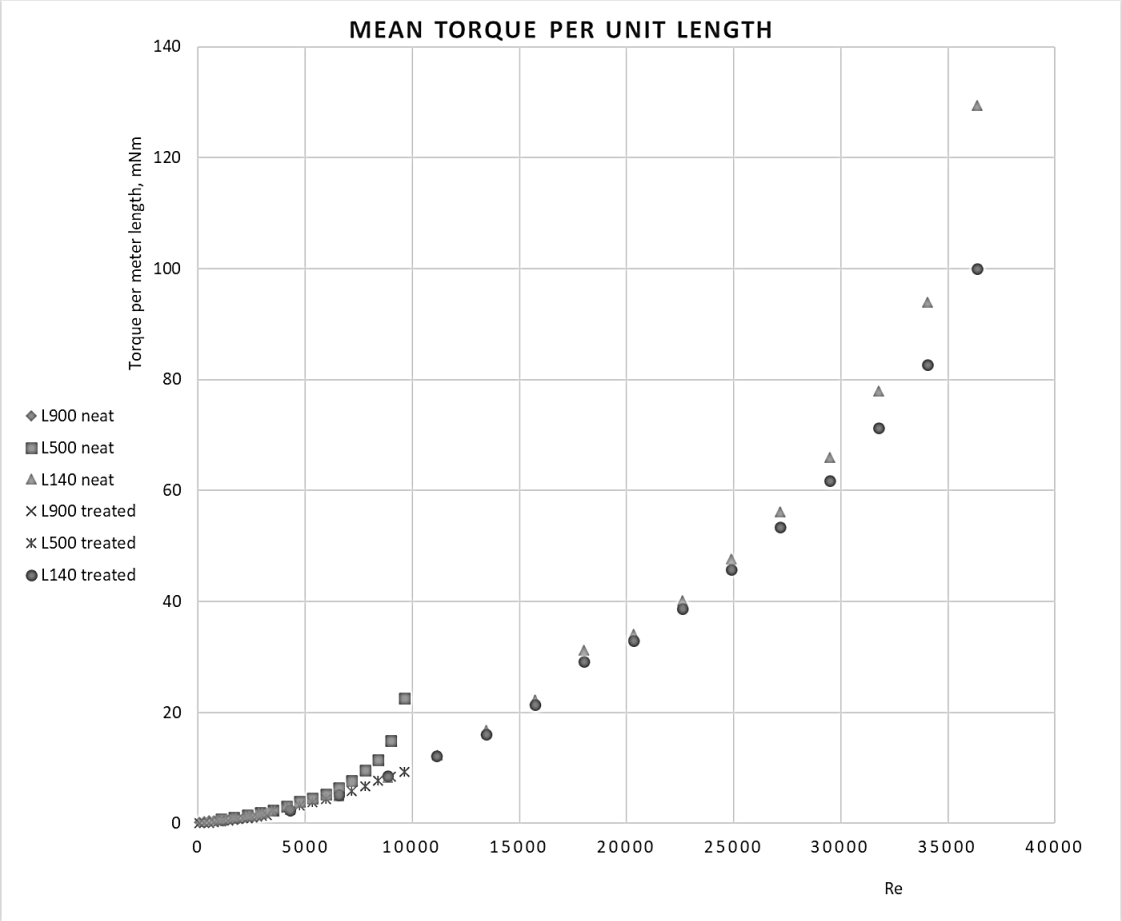

Figure 24. Torque per unit length for rotating non-treated and treated rotating cylinders

It is important to point out that this attempt to combine the results for all three aspect ratios is not explicitly accurate. It is due to differences in vibration characteristics that occur for varying lengths of the rotating suspended structures.

This shows that there is evidence that a drag reduction occurs for rotating disks and cylinders, but will it also apply to a moving vessel?

Chapter

6. Field Investigation: setup, results, and discussion

6.1. Introduction

The purpose of this experiment is to establish if the surface fabricated by the method described in section 3. 3. and applied to a marine vessel has the expected drag reducing ability in calm water.

6. 2. The towing tank experiment

6. 2. 1. Towing tank experimental setup.

The effects of the treated and the non-treated surfaces at linear motion and at a specifically marine application are studied in the towing tank experiment. For both the treated and non-treated hull surfaces, the drag reduction assessment is done by measuring and comparing the forces required for towing a boat model through calm water.

A ship's resistance components are discussed in section 4.5. of this thesis. The towing force represents the total resistance of the towed model. The skin friction is one component of the total resistance, and it is the subject of interest in this study. It is assumed, that if a difference in the total resistance for the same vessel with the treated and non-treated surfaces is detected, then it is, most likely, due to a change in the skin friction, since the hull shape is identical.

6. 2. 2. Ship model construction

The nature of the surface treatment requires an aluminium substrate. The easiest approach is to find an existing line set for a metal marine vehicle. Maxsurf is a software package for hull design equipped with naval architecture tools for the fairness, the optimisation and stress analysis. The package offers a number of examples designs of various marine vessels and a 31 m sample workboat was chosen.

The criteria include simplicity in means of construction and the need for surfaces to be developable i.e. able to be cut out of a flat aluminium sheet and wrapped in order to achieve the shape of the hull parts. “Workboat_2Surface_Developable” meets the criteria. The workboat model was scaled at a ratio of 1:25. Figure 25 shows the overall appearance of the hull as presented using Maxsurf. The model’s dimensions are:

Overall length, Loa	1.25 m
Length of waterline, Lwl	1.07 m
Overall beam, Boa	0.3 m
Waterline beam, Bwl	0.268 m
Hull height at midship, H	0.205 m
Draft, D	0.06 m
The wetted surface (according to Maxsurf calculations)	0.2441 m^2

Using the Maxsurf software, surfaces were conically developed and dxf-files for laser cutting were prepared.

The model was constructed of marine grade sheet aluminium (5083) at Unitec, Auckland, see Figure 26.

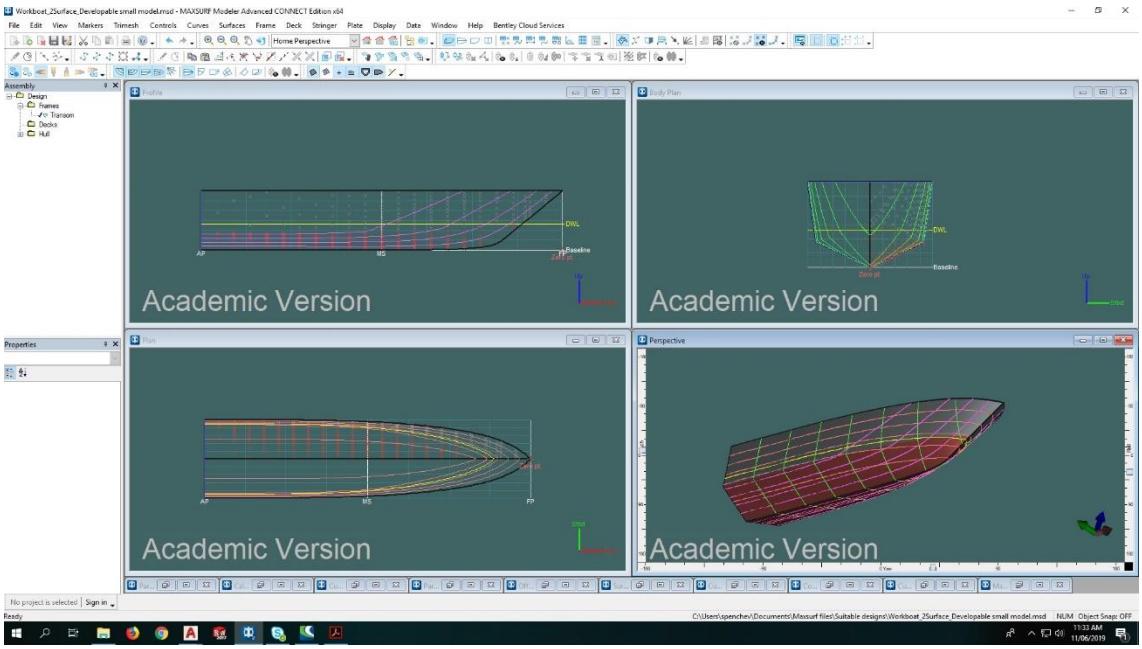

Figure 25. Workboat lines from the example design in Maxsurf.

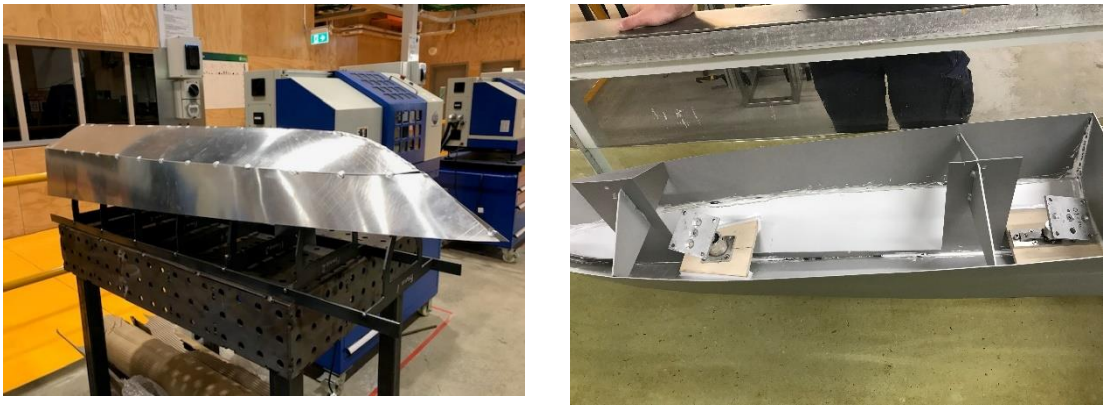

a. b.

Figure 26. Test boat: a. Model is tack-welded; b. Spherical joints are attached to the hull.

The welding of the hull produces some small deformations, which may affect the test results if two hulls are used which is the reason for testing same hull with and without the treatment.

The hull was anodised and sealed with boehmite by Alert Anodising (NZ) Ltd in Auckland. It was then shipped to the AMC Towing Tank in Launceston, Tasmania, where silicon oil was re-applied as described in section 3.2.

6. 2. 3. Ship model testing facility

The tests were conducted at the Australian Maritime Collage (AMC) Towing Tank in Launceston Tasmania, Australia, see Figure 27.

This facility has the following specification:

Dimensions: L 100m x W 3.55m

Water Depth: 1.5m

Carriage speed range: 0 to 4.6m/s

Ship model lengths: 1.0 to 3.0m

PC based data acquisition and processing

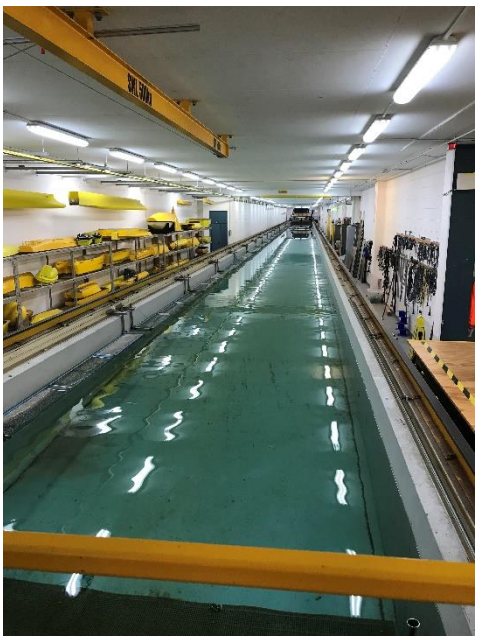

Figure 27. Towing tank at AMC, Tasmania

6. 2. 4. Towing test design

The towing tests include measuring the force required to tow the boat at a specific speed. The AMC, as a facility of great reputation, has an established protocol that is followed at all times. The carriage running along the basin is equipped with a towing rig containing two posts supporting the boat. The spherical joints and a vertical sliding configuration provide the freedom to set natural boat position in the water. Correct waterline is achieved by placing some ballast in the hull. This position sets initial location zero. The arrangement is equipped with a system that measures the horizontal towing force and other elements of the behaviour of the moving boat, such as sinkage, vertical change in the position in both supporting points. The change in this location is measured by the system giving full information at any defined speed of the carriage and boat. Figure 28 shows mounting system of the boat to the towing rig.

a. b.

Figure 28. a. Spherical joints attached to the boat, b. Vertical posts.

This installation allows assessing of the towing forces occurring on a naturally behaving vessel along its way, including the sinkage and the trim due to the viscous pressure forces.

The possible factors affecting results are analysed and controlled. These are:

- Surface tension of the calm water after sitting undisturbed for a long time. In order to avoid this effect, the first run for the day is not included into the data and is linked to Condition 0 in the overall results. This condition is part of the set-up rather than actual experimental run.

- Contamination of the surface of the water is another important factor. That is why skimming is performed and measured values before and after skimming, are included in the results for Condition 2. This condition is used to calculate repeatability of the results.

- Load cell errors are another source of inaccuracy. These are calibrated before and after each series of runs.

- Gradual increase or decrease of the velocity of the runs may affect the results as well. That is why the velocity for each run is randomly chosen i.e., jumping between the values.

- Alignment of the installation is another source of possible errors. This is the reason for mounting and dismounting the vessel repeatedly followed by load cell calibration under Condition 0. Comparing the results allows for an assessment of the effect of the alignment.

- Wash out of the Silicon oil may change the performance of the studied surface. Condition 4 includes re-application of the silicon oil. On the other hand, if the layer exceeds the optimum, it may have an adverse effect on the resistance due to a heavy intermediate layer.

The velocities of the experiment are decided in accordance with facility capabilities and safety. These are 1 m/s, 1.5 m/s, 2m/s, 2.5 m/s and 3 m/s. One hundred meters of run allows the development of a well-established water flow around the vessel at any of the velocities. More details about velocity and scaling are given in subsection 6. 2. 5.

Conditions under which the tests are conducted are as follows:

Condition 0 is a set up condition. This will include first run of the day, recalibration of the load cell, if needed, and skimming. If satisfactory, another condition is to be run.

Condition 1. All five velocities are performed subsequently; the first actual experimental data is derived.

Condition 2 is designed to reveal the consistency of the tests. The run velocities are applied in random manner.

Condition 3 is similar to Condition 2 but it is run after any re-alignment of the boat mounts.

Condition 4 is similar to Condition 2 but Silicon oil is re-applied to the surface of the hull. It means that a new alignment of the boat mounts has to be performed as well.

Condition 5 is the same as Condition 2 but the hull is stripped of its oil coating and paint is applied. Paint fills the pores of the surface.

6. 2. 5. Scaling in this experiment

The scaling is a process when the results from the model testing are transferred to a full-scale ship in order to predict its resistance. There are two ways of scaling -up. One way is to look for the same wave making conditions for the model and the full-size ship, and the other is to look for the same skin friction conditions for both.

The same wave making conditions or “sailing mode” occur when both will have same Froude number. Froude number, F_n, is defined by the following equation (80):

$$F_n = \frac{V}{\sqrt{gL}} \qquad (80)$$

where,

V, is the vessel velocity in m/s,

g, is the earth acceleration in m/s^2,

L, is the length of the waterline of the vessel in m.

Using subscripts 'model' for experimental boat and 'ship' for full-scale vessel, and expressing equality of the Froude numbers for both gives:

$$\frac{V_{model}}{\sqrt{gL_{model}}} = \frac{V_{ship}}{\sqrt{gL_{ship}}} \qquad (81)$$

The solution of equation (81) for V_{ship} will give the values of velocities corresponding to the velocities of the model at the same wave making conditions. It means that Residuary Coefficient C_R, is the same for both the model and full-scale vessel. Using this information, the Residuary Resistance of the full-scale vessel can be estimated.

The typical practice is to calculate Skin Friction Resistance for the full-scale ship at the current velocity and non-slip conditions, then is added to Residuary Resistance in order to estimate total resistance of the ship. (Lewis, 1988)

The above-mentioned method is the method used by naval architects to predict full-scale ship resistance. According to the scale ratio of the length of the model and the ship it is clear that the speed of the model will drop down when testing model in the towing tank.

In this study, the point of interest is skin friction, and the scaling of this sort is not helpful. In case we attempt to scale the model with idea to create same friction conditions i.e., same Reynolds number, the speed of the model has to be increased dramatically what is technically impractical. The result of such scaling is shown in Table 10, based on model

speed. While Froude scaling gives higher speeds for full-size ship, the Reynolds scaling gives much lower speeds.

For rough estimation it is used the same skin friction conditions for the model and full-scale ship occur if Reynolds number, equation (61), is the same for both. Using subscripts 'model' for experimental boat and 'ship' for full-scale vessel, and expressing equality of the Reynolds numbers for both gives:

$$\frac{V_{model}L_{model}}{\nu} = \frac{V_{ship}L_{ship}}{\nu} \qquad (82)$$

The solution of Equation (82) for V_{ship} will give the values of velocities corresponding to the velocities of the model at the same conditions for skin friction.

The scaled velocities by Froude and by Reynolds are computed and shown in Table 10.

Table 10. The speeds corresponding to the model velocities at Froude scaling and Reynolds scaling

Model velocity	Ship velocity	Ship velocity
	Froude scaling	Reynolds scaling
m/s	m/s	m/s
1	5	0.04
1.5	7.5	0.06
2	10	0.08
2.5	12.5	0.1
3	15	0.12

6. 2. 6. Towing tank experiment results and discussions

After running the experiments at conditions described in subsection 6. 2. 4., the acquired data was used to establish residual resistance for the non-treated model, where typical procedure is applied as follows:

a. The total towing force is measured
b. The skin friction resistance is calculated using Equations (64) and (62)
c. The calculated skin friction is subtracted from the total force; thus, the residual resistance for the model is derived.

Since same model is used non-treated and treated, it can be assumed that residual resistance is the same in both cases. It allows reversing the process for the treated model, i.e., the residual resistance is subtracted from the measured total resistance of the treated hull; thus, deriving the skin friction resistance and friction coefficient respectively.

The derived friction resistance and friction coefficient are each compared with the calculated one and applied to a full-scale vessel. Since the friction coefficient is derived for a specific Reynolds number, Reynolds's scaling is used.

The raw data from the tests show the forces applied to the model to tow it at a specific speed, the speed itself and the sinkage at the supporting posts. The latter allows reconstruction of the trim angle and sinkage using CAD software. The position of the vessel at each of the tested speeds and conditions in respect of the water surface gives information to compute the wetted surface correctly. An example of modelling of the boat's attitude is presented in Figure 29.

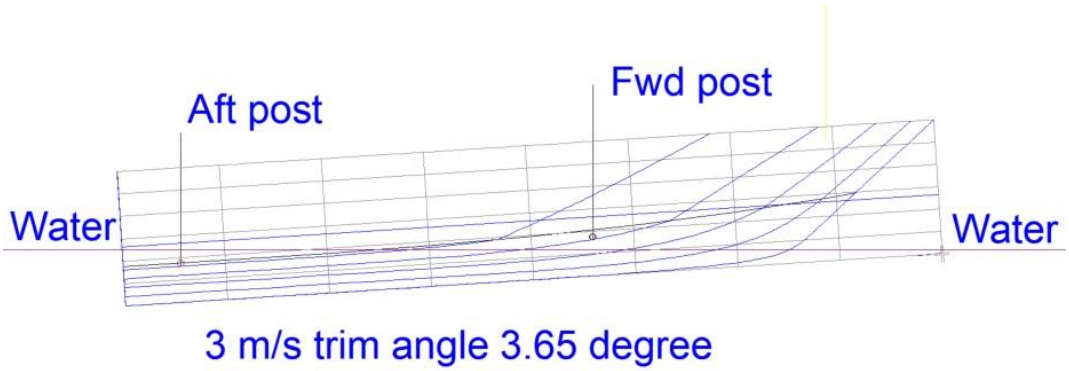

Figure 29. Boat attitude modelling.

Table 11 presents the mean values f**o**r the speeds (measured), the Reynolds numbers, the total resistance (measured), the wetted surface, the friction coefficient (calculated by Equation 64), the frictional resistance and residuary resistance.

Table 11. The mean values from measured and calculated quantities for the non-treated model boat.

Speeds (measured)	Reynolds numbers	Total resistance (measured)	Wetted surface	Friction coefficient	Friction resistance	Residuary resistance
m/s		N	m^2	$x10^{-3}$	N	N
1	1,085,671	2.3980	0.2485	4.6049	0.5641	1.8339
1.5	1,631,982	7.2105	0.3677	4.2261	1.7309	5.4796
2	2,178,157	13.6112	0.2627	3.9853	2.0774	11.5338
2.5	2,724,540	15.4746	0.2453	3.8125	2.9026	12.5720
3	3,269,601	17.6476	0.2395	3.6799	3.9402	13.7074

The order of the columns reflects the sequence of the calculations. That is why Table 12 showing same quantities but for treated model, is presented in a different order.

Table 12. The mean values from measured and calculated quantities for the treated model boat.

Speeds (measured)	Reynolds numbers	Total resistance (measured)	Residuary resistance	Friction resistance	Wetted surface	Friction coefficient
m/s		N	N	N	m^2	$x10^{-3}$
1	1,085,671	2.3544	1.8339	0.5205	0.2467	4.2813
1.5	1,631,982	7.1524	5.4796	1.6728	0.3654	4.0995
2	2,178,157	13.5350	11.5338	2.0012	0.2631	3.8343
2.5	2,724,540	15.3880	12.5720	2.8160	0.2464	3.6817
3	3,269,601	17.4054	13.7074	3.6980	0.2393	3.4566

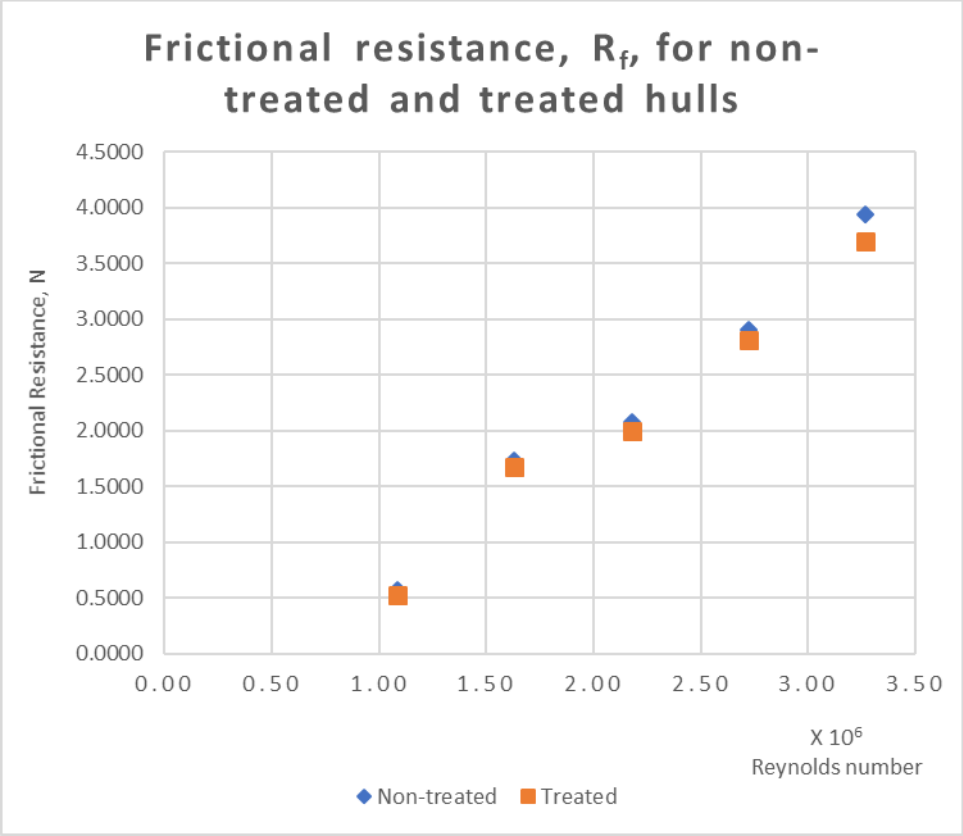

Figure 30. The mean values of the frictional resistance for non-treated and treated hull at varying Reynolds numbers.

The derived frictional resistance of non-treated and treated hulls is plotted and shown in Figure 30. The differences in the values are calculated (see Table 13) and the percentage of the change is expressed as equation (83).

$$Percentage\ change\ in\ R_F = \frac{R_{F\ non-treated} - R_{F\ treated}}{R_{F\ non-treated}} \times 100, \quad \% \qquad (83)$$

where, R_F is frictional resistance.

Table 13. Calculated difference in the mean of frictional resistance for non-treated and treated hull at different speeds.

Speed	R_{fnon}-R_{ftr}	% change
m/s	N	%
1	0.0436	7.73
1.5	0.0581	3.36
2	0.0762	3.67
2.5	0.0866	2.98
3	0.2422	6.15

It is important to assess the consistency of the experimental series. The towing speed of 2 m/s is used for this purpose. These experiments are run 12 times at different conditions as described in subsection 6. 2. 4. Based on the data from these extra runs, the standard deviation is calculated using equation (68). The derived value of the standard deviation is 0.078 N.

The standard deviation of the measured force is 0.58 % of its value. This shows a very robust consistency of the experimental results.

On the other hand, considering the difference in the frictional resistance at speed of 2 m/s being 0.0762 ± 0.078 N the gain of 3% is applied for the mean values only. The

actual range of possible values of the frictional resistance gain is from – 0.0018 N to 0.1542 N. The interpretation of such data would be that there is little to no effect.

While it is correct for most of the testing speeds, 3 m/s is an exception. The calculated difference in the measured resistance is 6% ± 2.8%. It shows a significant gain ranged from 3.2% to 8%. The possible reason for this dramatic change is in the planning mode of the vessel (Froude number 0.9) where part of the wetted surface is not under solid sheet of water but a mixture of air and water, i.e., spray. SLIPS performance in this environment can be different and should be the subject of further study.

Still, let us assume a gain of 3% in frictional resistance for treated hull and consider full-scale vessel. For 2 m/s speed of the model, corresponding scaled speed of the ship is 0.08 m/s. At this speed, frictional coefficient for the full-scale vessel is the same as for the model, i.e. it can be used for calculation of the frictional resistance of the ship. For non-treated hull, C_F is 0.003985 and for treated, C_F is 0.003834, see Tables 11 and 12. Wetted surface of the full-scale ship is calculated (152.5 m^2) and Equation (62) is applied.

The results are as follows

R_F = 1.9417 N for non-treated ship and

R_F = 1.8681 N for treated ship

The frictional resistance reduction is 3.7 %.

On the other hand, frictional resistance is only a fraction of the total resistance which can be different depending on the sailing mode i.e. displacement, semi displacement or planing. Any one of them is possible due to the flat surfaces of the chosen boat and the light construction. Estimation of the sailing mode is done by Froude number, Equation

(80). In this case, it is 0.024. This is significantly less than 0.4, a displacement mode is therefore defined.

Generally, for slow cargo ships, frictional resistance could be up to 70-80% of the total resistance but for high-speed vessels, it may be less than 40%. In the considered sea craft at low speeds, it will be fair to assume about 35-40% (Larsson & Eliasson, 2000). With increase of speed, it will drop even more.

With the above considerations, frictional resistance reduction of 3.7% translates to the total resistance reduction of 1% to 1.5% at the best for this type of vessel.

Chapter

7. Conclusions and Future Research Recommendations

7. 1. Introduction

This chapter is dedicated to the summary and conclusions drawn along this study. It begins with surface preparation in order to achieve SLIPS. It follows by the quick primary assessment for drag reduction of the prepared SLIPS, tested by rotating disk experiment.

The next are summary and conclusions from rotating cylinder experiments. It reveals limitations of the study and identifies phenomena observed along the experimental work. Section 7. 2 finishes by towing tank experiments summarizing the results and drawing conclusions.

The chapter ends with future research recommendations. This section comprises various areas like theoretical development for slip condition, SLIPS in condition of vibration, effect of SLIPS for drag reduction in air and/or water spray and full-scale ship experiments when SLIPS is applied.

7. 2. Conclusions

This study focuses on use of SLIPS for marine applications. The work investigates its effect on surface-water interaction at varying regimes of flow, as well as on the overall resistance of the ship.

The studied Slippery Lubricant Infused Porous Surface is based on the principles, suggested by Philseok Kim. While the pores in Kim's work are about 50 μm and larger,

an anodised surface offers pores of 10 - 20 µm and smaller, i.e. it is a finer structure. A boehmite nano structure is on a scale of 20-30 nm and the adhesion of silicon oil to that structured surface has not been studied yet and this is an area for future investigation.

The newly developed SLIPS was tested for drag reduction in the laboratory and proven worthy to continue testing it for marine application.

In a laboratory study, the initial rotating disk tests showed 3-4.7% in drag reduction. Standard deviation of the measured torque is within the range of 0.9% to 1.2 % of the measured value and indicates good consistency of the experimental data.

The assumption that the drag reduction is due to the slip leads to new conditions for the Navier-Stokes and continuity differential equations (13), (14), (15) and (17). This system of equations can be solved for boundary conditions where z = - s, s is slip, (see page 18 for definition), and where Ur = 0, Uφ = r, Uz = 0.

Rotating coaxial cylinders experiment was conducted at three aspect ratios aiming to comprise wider range of Reynolds numbers using same apparatus. The diameter of the inner cylinder and the gap was maintained the same.

These tests showed up to 40% drug reduction for laminar or predominately laminar flow dropping to 3% once turbulence developed, reaching rotational Reynolds number of 2700.

At higher Reynolds numbers, further drop of SLIPS drag reducing effect was observed reaching no benefit at all. Measurements below 10% of the capacity of the device were excluded since they are considered unreliable according to the manufacturer.

On the other hand, change in torque required to rotate cylinders for non-treated and treated cylinders is not dropping steadily down but shows increase and decrease of the

effect of SLIPS with increase of Reynolds number. This coincides with the development of surface waves in the gap and induced vibration.

Due to the difference in the length of the cylinders, vibration characteristics are not the same for different aspect ratio. Thus, the combined plot for required torque per unit length for rotating non-treated and treated rotating cylinders is challenging and indicative only (Figure 24).

This study shows that in situation of vibration there is a significant drop in the required torque for SLIPS, up to 50%. It has to be admitted that vibration itself is a significant change in the flow conditions. That is why it requires special investigation.

Marine application of SLIPS was studied by testing a boat model in the towing tank facility at Australian Maritime Collage in Launceston. A model of a 31 m workboat was constructed of aluminium alloy 5083. It was tested at various speeds both treated and non-treated for Reynolds number between 1,085,000 and 3,269,000.

Although the difference in the friction resistance of mean values indicates 3.5% drag reduction, it is within the 3.8% standard deviation of the measured values. It can be concluded that there is little (3.5%) to no effect.

At planing mode, however, where friction resistance consists of resistance from solid water sheet and sprays, a significant improvement of 6% in towing force is observed. This shows that area of potential application of the treatment is aluminium-planing vessels.

An attempt to predict full-scale ship drag reduction was made. It resulted in an estimation of possible total drag reduction from 0 to 1.5%. This prediction is based on very broad assumptions and applicable for displacement mode at low speed. Planing mode, where friction resistance from sprays is involved is not included.

7. 3. Future Research Recommendation

7. 3. 1. Vibration as a factor

Along with the work on this topic, number of phenomena were observed and recorded. These were accompanied with questions that are a basis for further study.

In the rotating coaxial cylinders experiments, whenever vibration was observed, drag reduction increased. Does vibration of SLIPS generate less vorticity compared with non-treated surfaces? It is a subject for further investigation.

7. 3. 2. Spray-surface interaction

In the towing tank experiment for 3 m/s speed of the model, drag reduction jumped to 6% at standard deviation of measured quantities of 2.8%. This is significant compared with lower speeds. The corresponding Froude number in this case is 0.9. It indicates that, in this case, the spray-affected surface area increased. This area is not under solid water sheet but under mixture of water and air. Investigation of the effect of SLIPS on drag reduction in air and air-water mixture is also a possible area of further study.

7. 3. 3. Full size ship test

The estimation of the effect of SLIPS in full-scale ship cannot be very accurately determined due to the differences in the sailing modes of the model and full-size ship. One is in planing mode; the other is in displacement mode. It would be beneficial to the study an up-scaled small aluminium vessel and test it in the real world.

7. 3. 4. Theoretical work and other options

Some theoretical work can be done for future tests by solving Navier-Stokes and continuity equations for slip conditions.

Although, the drag reduction is small for these particular SLIPS, more surface types can be investigated with possible combination of riblets or other microstructures and/or lubricants to achieve better results.

References

Batchelor, G. K. (1985). *An Introduction to Fluid Dynamics*: Cambridge University Press.

Baudry, J., Charlaix, E., Tonck, A., & Mazuyer, D. (2001). Experimental evidence for a large slip effect at a nonwetting fluid-solid interface. *Langmuir, 17*(17), 5232-5236.

Berg, S., Cense, A., Hofman, J., & Smits, R. (2008). Two-phase flow in porous media with slip boundary condition. *Transport in Porous Media, 74*(3), 275-292.

Bhushan, B. (2012). *Biomimetics: Bioinspired Hierarchical- Structured Surfaces for Green Science and Technology*. Berlin, Heidelberg: Springer Berlin Heidelberg, Berlin, Heidelberg.

Bixler, G. D., & Bhushan, B. (2013). Fluid Drag Reduction with Shark-Skin Riblet Inspired Microstructured Surfaces. *Advanced Functional Materials, 23*(36), 4507-4528. doi: 10.1002/adfm.201203683

Blake, T. D. (1990). Slip between a liquid and a solid: DM Tolstoi's (1952) theory reconsidered. *Colloids and surfaces, 47*, 135-145.

Brockman, M. R. (1957). Resistance of Flow in Teflon and Brass Tubes *Journal of the National Bureau of Standards, 58*(1), 10.

BROOKFIELD. (n.d). BROOKFIELD DIAL READING VISCOMETER

with Electronic Drive *Operating Instructions*

Manual No. M00-151-H0612.

Bunkin, N., Kiseleva, O., Lobeyev, A., Movchan, T., Ninham, B., & Vinogradova, O. (1997). Effect of salts and dissolved gas on optical cavitation near hydrophobic and hydrophilic surfaces. *Langmuir, 13*(11), 3024-3028.

Bushnell, D. M., Hefner, J. N., & ebrary Inc. (1990). *Viscous drag reduction in boundary layers*. Washington, D.C.: American Institute of Aeronautics and Astronautics Inc.

Busse, A., Sandham, N. D., McHale, G., & Newton, M. I. (2013). Change in drag, apparent slip and optimum air layer thickness for laminar flow over an idealised superhydrophobic surface. *Journal of Fluid Mechanics, 727*, 488-508.

Carlton, J. (2007). *Marine propellers and propulsion* (2nd ed.). Amsterdam ; Oxford: Elsevier Butterworth-Heinemann.

Chamorro, L. P., Arndt, R., & Sotiropoulos, F. (2013). Drag reduction of large wind turbine blades through riblets: Evaluation of riblet geometry and application strategies. *Renewable energy, 50*, 1095-1105.

Chandler, D. (2007). Physical chemistry: Oil on troubled waters. *Nature, 445*(7130), 831-832.

Chen, H., Rao, F., Shang, X., Zhang, D., & Hagiwara, I. (2013). Biomimetic Drag Reduction Study on Herringbone Riblets of Bird Feather. *Journal of Bionic Engineering, 10*(3), 341-349. doi: http://dx.doi.org/10.1016/S1672-6529(13)60229-2

Childs, P. R. N. (2011). Chapter 6 - Rotating Cylinders, Annuli, and Spheres *Rotating Flow* (pp. 177-247). Oxford: Butterworth-Heinemann. doi:http://dx.doi.org/10.1016/B978-0-12-382098-3.00006-8

Childs, P. R. N. (2011). Rotating Flow *Rotating Flow* (pp. 383-389). Oxford: Butterworth-Heinemann. doi:https://doi.org/10.1016/B978-0-12-382098-3.00017-2

Choi, C.-H., & Kim, C.-J. (2006). Large Slip of Aqueous Liquid Flow over a Nanoengineered Superhydrophobic Surface. *Physical Review Letters, 96*(6), 066001.

Choi, C.-H., Westin, K. J. A., & Breuer, K. S. (2003). Apparent slip flows in hydrophilic and hydrophobic microchannels. *Physics of Fluids (1994-present), 15*(10), 2897-2902.

Churaev, N., Sobolev, V., & Somov, A. (1984). Slippage of liquids over lyophobic solid surfaces. *Journal of Colloid and Interface Science, 97*(2), 574-581.

Cochran, W. G. (1934). The flow due to a rotating disc. *Proceedings Cambridge Phil. Society,, 30*, 365–375.

Cottin-Bizonne, C., Barentin, C., Charlaix, É., Bocquet, L., & Barrat, J.-L. (2004). Dynamics of simple liquids at heterogeneous surfaces: molecular-dynamics simulations and hydrodynamic description. *The European Physical Journal E, 15*(4), 427-438.

Cottin-Bizonne, C., Barrat, J.-L., Bocquet, L., & Charlaix, E. (2003). Low-friction flows of liquid at nanopatterned interfaces. *Nat Mater, 2*(4), 237-240.

Cottin-Bizonne, C., Cross, B., Steinberger, A., & Charlaix, E. (2005). Boundary slip on smooth hydrophobic surfaces: Intrinsic effects and possible artifacts. *Physical review letters, 94*(5), 056102.

Daniello, R. J., Waterhouse, N. E., & Rothstein, J. P. (2009). Drag reduction in turbulent flows over superhydrophobic surfaces. *Physics of Fluids (1994-present), 21*(8), 085103.

Deen, W. M. (1998). *Analysis of transport phenomena (topics in chemical engineering)* (Vol. 3): Oxford University Press, New York.

Doshi, D. A., Watkins, E. B., Israelachvili, J. N., & Majewski, J. (2005). Reduced water density at hydrophobic surfaces: effect of dissolved gases. *Proceedings of the National Academy of Sciences of the United States of America, 102*(27), 9458-9462.

Eckhardt, B., Grossmann, S., & Lohse, D. (2007). Torque scaling in turbulent Taylor-Couette flow between independently rotating cylinders. *Journal of Fluid Mechanics, 581*, 221.

Edwards, J. (1997). *Coating and surface treatment systems for metals : a comprehensive guide to selection*. Materials Park, Ohio ; Stevenage, Hertfordshire: Materials Park, Ohio ; Stevenage, Hertfordshire : ASM International ; Finishing Publications 1997.

Foeth, E. J., Eggers, R. & Quadvlieg F.H.H.A. (2010). *The efficacy of air-bubble lubrication for decreasing friction resistance.* Paper presented at the International Conference on Ship Drag Reduction SMOOTH-SHIPS, Istanbul, Turkey. Retrieved from http://cleantech.cnss.no/wp-content/uploads/2011/05/2010-Foeth-et-al-The-efficacy-of-air-bubble-lubrication-for-decreasing-friction-resistance1.pdf

Fujimtsu, N. (2013). *Direct numerical simulation on drag reduction of chnnel flow with visco-elastic wall.* Paper presented at the 51st AIAA Aerospace Sciences Meeting including the New Horizons Forum and Aerospace Exposition Retrieved from

Fukuda, K., Tokunaga, J., Nobunaga, T., Nakatani, T., Iwasaki, T., & Kunitake, Y. (2000). Frictional drag reduction with air lubricant over a super-water-repellent surface. *Journal of Marine Science and Technology, 5*(3), 123-130. doi: 10.1007/s007730070009

Gad-el-Hak, M. (2002). Compliant coatings for drag reduction. *Progress in Aerospace Sciences, 38*(1), 77-99. doi: http://dx.doi.org/10.1016/S0376-0421(01)00020-3

Gregory, N., Stuart, J.T., andWalker, W.S. . (1955). On the stability of three dimensional boundary layers with application to the flow due to a rotating disc. *Philosophical Transactions of the Royal Society*(248), 155-198.

Horn, R. G., Vinogradova, O. I., Mackay, M. E., & Phan-Thien, N. (2000). Hydrodynamic slippage inferred from thin film drainage measurements in a solution of nonadsorbing polymer. *The Journal of Chemical Physics, 112*(14), 6424-6433.

Israelachvili, J. N. (1992). Intermolecular and surface forces: with applications to colloidal and biological systems (Colloid Science): Academic press London.

Jin, S., Huang, P., Park, J., Yoo, J., & Breuer, K. (2004). Near-surface velocimetry using evanescent wave illumination. *Experiments in fluids, 37*(6), 825-833.

Joly, L., Ybert, C., & Bocquet, L. (2006). Probing the nanohydrodynamics at liquid-solid interfaces using thermal motion. *Physical review letters, 96*(4), 046101.

Joseph, P., & Tabeling, P. (2005). Direct measurement of the apparent slip length. *Physical Review E, 71*(3), 035303.

Jung, Y. C., & Bhushan, B. (2009). Biomimetic structures for fluid drag reduction in laminar and turbulent flows. *Journal of Physics: Condensed Matter, 22*(3), 035104.

Karman, T. v. (1921). Über laminare und turbulente reibung [on laminar and turbulent friction]. *Zeitschrift für angewandte Mathematik Mechanik, 1*, 233–252.

Kim, P., Kreder, M. J., Alvarenga, J., & Aizenberg, J. (2013a). Hierarchical or not? Effect of the length scale and hierarchy of the surface roughness on omniphobicity of lubricant-infused substrates. *Nano Lett, 13*(4), 1793-1799. doi: 10.1021/nl4003969

Kim, P., Kreder, M. J., Alvarenga, J., & Aizenberg, J. (2013b). Hierarchical or Not? Effect of the Length Scale and Hierarchy of the Surface Roughness on Omniphobicity of Lubricant-Infused Substrates. *Nano Lett, 13*(4), 1793-1799. doi: 10.1021/nl4003969

Kunz, R. F., Maxey, M. R., Tryggvason, G., Fontaine, A. A., Ceccio, S. L., Gibeling, H. J., & Petrie, H. L. (2006). Validation of Two-Fluid Eulerian CFD Modeling for Microbubble Drag Reduction Across a Wide Range of Reynolds Numbers. *Journal of Fluids Engineering, 129*(1), 66-79. doi: 10.1115/1.2375124

Larsson, L., & Eliasson, R. E. (2000). *Principles of yacht design* (2nd ed.). London: Adlard Coles Nautical.

Lathrop, D. P., Fineberg, J., & Swinney, H. L. (1992). Transition to shear-driven turbulence in Couette-Taylor flow. Physical review. *Phys Rev A. Atomic, molecular, and optical physics 46(10)*, 6390–6405. doi: 10.1103/physreva.46.6390.

Lauga, E., & Stone, H. A. (2003). Effective slip in pressure-driven Stokes flow. *Journal of Fluid Mechanics, 489*, 55-77.

Lee, C., Choi, C.-H., & Kim, C.-J. C. (2008). Structured Surfaces for a Giant Liquid Slip. *Physical Review Letters, 101*(6), 064501.

Lee, C., & Kim, C.-J. C. (2009). Maximizing the Giant Liquid Slip on Superhydrophobic Microstructures by Nanostructuring Their Sidewalls. *Langmuir, 25*(21), 12812-12818. doi: 10.1021/la901824d

Lewis, E. V. (1988). *Principles of naval architecture* (2nd rev ed ed.). Jersey City, NJ: Society of Naval Architects and Marine Engineers.

Majeed, M. H. J. A.-N. J. f. E. S. (2014). Static Contact Angle and Large Water Droplet Thickness Measurements with the Change of Water Temperature. *17*, 114-128.

Migler, K., Hervet, H., & Leger, L. (1993). Slip transition of a polymer melt under shear stress. *Physical review letters, 70*(3), 287.

Montgomery, D. C. (2018). *Applied statistics and probability for engineers*. Retrieved from http://ebookcentral.proquest.com/lib/AUT/detail.action?docID=5633334

Murai, Y., Fukuda, H., Oishi, Y., Kodama, Y., & Yamamoto, F. (2007). Skin friction reduction by large air bubbles in a horizontal channel flow. *International Journal of Multiphase Flow, 33*(2), 147-163. doi: http://dx.doi.org/10.1016/j.ijmultiphaseflow.2006.08.008

Muralidhar, F., Daniello, Rothstein, Jonathan (2011). Influence of slip on the flow past superhydrophobic circular cylinders. *Journal of Fluid Mechanics, 680*, 459-476. doi: doi:10.1017/jfm.2011.172

Navier, C. (1823). Mémoire sur les lois du mouvement des fluides. *Mémoires de l'Académie Royale des Sciences de l'Institut de France, 6*, 389-440.

Osborn, J. H. (2014).

Understanding and Specifying Anodizing:what a Manufacturer Needs to Know…. Retrieved from http://www.omwcorp.com/understandingano/anoindex.html

Owen, J. M., and Rofers,R.H. . (1989). Flow and heat transfer in rotating-disc systems. *1*.

Park, H., Sun, G., & Kim, C.-J. C. (2014). Superhydrophobic turbulent drag reduction as a function of surface grating parameters. *Journal of Fluid Mechanics, 747*, 722-734. doi: doi:10.1017/jfm.2014.151

Peguero, C., & Breuer, K. (2009). On drag reduction in turbulent channel flow over superhydrophobic surfaces *Advances in Turbulence XII* (pp. 233-236): Springer.

Phillips-Birt, D. (1970). *Ship model testing* (Vol. Leonard-Hill).

Pit, R., Hervet, H., & Léger, L. (1999). Friction and slip of a simple liquid at a solid surface. *Tribology Letters, 7*(2-3), 147-152. doi: 10.1023/A:1019161101812

Priezjev, N. V., & Troian, S. M. (2004). Molecular origin and dynamic behavior of slip in sheared polymer films. *Physical review letters, 92*(1), 018302.

Priezjev, N. V., & Troian, S. M. (2006). Influence of periodic wall roughness on the slip behaviour at liquid/solid interfaces: molecular-scale simulations versus continuum predictions. *Journal of Fluid Mechanics, 554*, 25-46.

Quéré, D. (2005). Non-sticking drops. *Reports on Progress in Physics, 68*(11), 2495.

Recktenwald, A., Lücke, M., & Müller, H. W. (1993). Taylor vortex formation in axial through-flow: Linear and weakly nonlinear analysis. *Physical Review E, 48*(6), 4444-4454.

Reif, W., & Dinkelacker, A. (1982). Hydrodynamics of the squamation in fast swimming sharks. *Neues Jahrbuch für Geologie und Palaeontologie, Abhandlungen, 164*, 184-187.

Rothstein, J. P. (2010). Slip on Superhydrophobic Surfaces *Annual Review of Fluid Mechanics* (Vol. 42, pp. 89-109). doi:10.1146/annurev-fluid-121108-145558

Schetz, J. A. a. F., A. E. . (1999). *Fundamentals of Fluid Mechanics* (3rd ed.): New York, NY [u.a.] : Wiley,.

Schnell, E. (1956). Slippage of water over nonwettable surfaces. *Journal of Applied Physics, 27*(10), 1149-1152.

Schönecker, C., Baier, T., & Hardt, S. (2014). Influence of the enclosed fluid on the flow over a microstructured surface in the Cassie state. *Journal of Fluid Mechanics, 740*, 168-195.

Schönecker, C., & Hardt, S. (2013). Longitudinal and transverse flow over a cavity containing a second immiscible fluid. *Journal of Fluid Mechanics, 717*, 376-394.

Schönecker, C., & Hardt, S. (2015). Assessment of drag reduction at slippery, topographically structured surfaces. *Microfluidics and Nanofluidics, 19*(1), 199-207.

Sherazi, T. A. (2016). Graft Polymerization. In E. Drioli & L. Giorno (Eds.), *Encyclopedia of Membranes* (pp. 886-887). Berlin, Heidelberg: Springer Berlin Heidelberg. doi:10.1007/978-3-662-44324-8_274

Smith, J. D., Dhiman, R., Anand, S., Reza-Garduno, E., Cohen, R. E., McKinley, G. H., & Varanasi, K. K. (2013). Droplet mobility on lubricant-impregnated surfaces. *Soft Matter, 9*(6), 1772-1780.

Solomon, B. R., Khalil, K. S., & Varanasi, K. K. (2014). Drag Reduction using Lubricant-Impregnated Surfaces in Viscous Laminar Flow. *Langmuir, 30*(36), 10970-10976. doi: 10.1021/la5021143

). Stockholm Convention. (Retrieved from http://chm.pops.int/Home/tabid/2121/Default.aspx

Sverchkov, A. V. (2010). *Application of air cavities on high-speed ships in Russia.* Paper presented at the INTERNATIONAL CONFERENCE ON SHIP DRAG REDUCTION (SMOOTH-Ships) Instanbul. Retrieved from http://202.114.89.60/resource/pdf/6478.pdf

Theodorcen, T. a. T., A. . (1944). Experiments on drag of revolving discs, xylinders and streamline fods at high speeds. *Naca Report 793*.

Thompson, P. A., & Troian, S. M. (1997). A general boundary condition for liquid flow at solid surfaces. *Nature, 389*(6649), 360-362.

Tolstoi, D. M. (1952). Molecular theory for slippage of liquids over solid surfaces. *Dokl Akad Nauk SSSR, 85*, 1089-1092 (In Russian).

Tretheway, D. C., & Meinhart, C. D. (2002). Apparent fluid slip at hydrophobic microchannel walls. *Physics of Fluids (1994-present), 14*(3), L9-L12.

Ünal, U., Ünal, B., & Atlar, M. (2012). Turbulent boundary layer measurements over flat surfaces coated by nanostructured marine antifoulings. *Experiments in Fluids, 52*(6), 1431-1448. doi: 10.1007/s00348-012-1262-z

Vinogradova, O. I. (1995). Drainage of a thin liquid film confined between hydrophobic surfaces. *Langmuir, 11*(6), 2213-2220.

Walsh, M., & Weinstein, L. (1978). *Drag and heat transfer on surfaces with small longitudinal fins.* Paper presented at the 11th Fluid and Plasma Dynamics Conference. Retrieved from

Walsh, M. J. (1980). Drag characteristics of V-groove and transverse curvature riblets.

Walsh, M. J. (1982). *Turbulent boundary layer drag reduction using riblets.* Paper presented at the AIAA, Aerospace Sciences Meeting. Retrieved from

Watanabe, U. Y., Udagawa H. (1999). Drag reduction of Newtonian fluid in a circular pipe with a highly water-repellent wall. *Journal of Fluid Mechanics, 381*, 225-238. doi: doi:10.1017/S0022112098003747

Wen, L., Weaver, J. C., & Lauder, G. V. (2014). Biomimetic shark skin: design, fabrication and hydrodynamic function. *Journal of Experimental Biology, 217*(10), 1656-1666.

Woo Yang, J., Park, H., Hwan Chun, H., Ceccio, S. L., Perlin, M., & Lee, I. (2014). Development and performance at high Reynolds number of a skin-friction reducing marine paint using polymer additives. *Ocean Engineering, 84*(0), 183-193. doi: http://dx.doi.org/10.1016/j.oceaneng.2014.04.009

Woolford, B., Prince, J., Maynes, D., & Webb, B. (2009). Particle image velocimetry characterization of turbulent channel flow with rib patterned superhydrophobic walls. *Physics of Fluids (1994-present), 21*(8), 085106.

Wu, Y., Cai, M., Li, Z., Song, X., Wang, H., Pei, X., & Zhou, F. (2014). Slip flow of diverse liquids on robust superomniphobic surfaces. *Journal of Colloid and Interface Science, 414*(0), 9-13. doi: http://dx.doi.org/10.1016/j.jcis.2013.09.041

Ybert, C., Barentin, C., Cottin-Bizonne, C., Joseph, P., & Bocquet, L. (2007). Achieving large slip with superhydrophobic surfaces: Scaling laws for generic geometries. *Physics of Fluids (1994-present), 19*(12), 123601.

Yuan, Y., & Lee, T. R. (2013). Contact angle and wetting properties *Surface science techniques* (pp. 3-34): Springer.

Zhu, Y., & Granick, S. (2001). Rate-dependent slip of Newtonian liquid at smooth surfaces. *Physical review letters, 87*(9), 096105.